

High-Order Curvilinear Finite Element Magneto-Hydrodynamics I: A Conservative Lagrangian Scheme

Jan Nikl^{a,b,c,*}, Milan Kuchařík^c, Stefan Weber^{a,d}

^a*ELI Beamlines Centre, Institute of Physics, Czech Academy of Sciences, 25241 Dolní Břežany, Czech Republic*

^b*Institute of Plasma Physics, Czech Academy of Sciences, 18200 Prague, Czech Republic*

^c*Faculty of Nuclear Sciences and Physical Engineering, Czech Technical University in Prague, 11519 Prague, Czech Republic*

^d*School of Science, Xi'an Jiaotong University, 710049 Xi'an, China*

Abstract

Magneto-hydrodynamics is one of the foremost models in plasma physics with applications in inertial confinement fusion, astrophysics and elsewhere. Advanced numerical methods are needed to get an insight into the complex physical phenomena. The classical Lagrangian methods are typically limited to the low orders of convergence and suffer from violation of the divergence-free condition for magnetic field or conservation of the invariants. In this paper, a multi-dimensional conservative high-order resistive magneto-hydrodynamic method based on curvilinear finite elements is presented. The condition on zero divergence of magnetic field and conservation of mass, momentum, magnetic flux and the total energy are satisfied exactly. The curvilinear elements prevent entangling of the computational mesh and its imprinting into the solution. A high-order conservative time integration is applied, where an arbitrary order of convergence is attained for problems of ideal magneto-hydrodynamics. Description of the method is given and multiple test problems demonstrating properties of the scheme are performed. The construction of the method and possible future directions of development are discussed.

Keywords: resistive magneto-hydrodynamics, Lagrangian hydrodynamics, high-order methods, finite element method, curvilinear meshes, conservative methods

1. Introduction

The magneto-hydrodynamic description is one of the major directions in plasma physics research. It plays a central and indispensable role in such as design of fusion devices or astrophysics and many others. We are particularly interested in the Lagrangian approach, where the coordinate system follows the flow of the fluid. It is mostly favored in areas of modeling where the medium undergoes extreme compression or expansion like inertial confinement fusion [1, 2], Z-pinch [3], supernovae collapses [4], cosmic jets [5], prepulse effects of ultra-intense lasers [6, 7] or laser ion acceleration beamlines [8, 9, 10] as are explored at facilities like ELI Beamlines [11, 12] and other multi-PW laser systems worldwide [13].

Efficient and accurate numerical tools are then needed for simulations of the physical phenomena occurring within these processes. However, the classical methods for resistive magneto-hydrodynamics (RMHD) are typically limited to low orders of convergence. New high-order methods are slowly appearing for the Eulerian approach [14, 15], but the literature is scarce for Lagrangian methods. A change of the paradigm comes with application of the finite element method (FEM) [16], which offers generality of the formulation in the mesh topology and also order of the elements. Although the latter option is not pursued by the authors due to the limitations in time integration and conservation properties primarily, another advantage of the design presents itself. The edge-centered elements equipped with an appropriate transformation rule

*Corresponding author

Email address: jan.nikl@eli-beams.eu (Jan Nikl)

perfectly suit the magnetic field discretization and exactly satisfy the divergence-free constraint, which poses a serious problem in numerical MHD [17]. Another milestone presents the development of the conservative high-order hydrodynamics based on the curvilinear finite elements [18], which introduced geometric mass conservation for the curved elements and an arbitrary order of convergence in space given by the polynomial order of the elements. However, conservative time stepping was still limited to the second order only and formulation of MHD was missing. Later, a convenient formulation of conservative Lagrangian MHD was developed for the staggered discretization [3]. Although limited to the second order and only to the transverse component of the magnetic field in 2D, the methodology is compatible with the finite element hydrodynamics.

This paper continues in these efforts and presents a multi-dimensional conservative high-order resistive magneto-hydrodynamics based on the curvilinear finite elements. Mass, momentum, magnetic flux and the total energy are conserved exactly. In addition, the divergence-free condition for the magnetic field is maintained exactly. Generality of the formulation allows to apply it on unstructured meshes, though the numerical examples are presented only for regular quadrilateral/hexahedral meshes. Together with a conservative high-order time integration, the numerical scheme attains an arbitrary order of convergence for ideal MHD problems theoretically. The implementation is part of the multi-physics code PETE2 [19], which continues our previous efforts [20, 21].

The remainder of the paper is organized as follows. A brief introduction to the physical model and the governing equations of RMHD are given in section 2. The numerical scheme is then described in section 3, starting from the weak formulation of the problem (section 3.1) and continuing with the discretization in space (section 3.2) to the fully discrete model (section 3.3). Next, the numerical method is validated and benchmarked on a set of test problems in section 4. A short discussion of benefits and limitations of the model is given in section 5, followed by concluding remarks in section 6. The future directions of this series of papers about high-order numerical MHD are outlined.

2. Physical model

Within the classical resistive magneto-hydrodynamics, the physical system is described as a magnetized fluid with the mass density ρ , mass-averaged velocity \vec{u} and specific internal energy ε . Its dynamics is modeled by the Euler equations, which are complemented by Faraday's law for the self-consistent magnetic field \vec{B} . In the Lagrangian formulation, they take the following integral form [3]:

$$\frac{d}{dt} \int_V \rho dV = 0, \quad (1a)$$

$$\frac{d}{dt} \int_V \rho \vec{u} dV = \oint_{\partial V} (\vec{\sigma} + \vec{\sigma}_B) \cdot d\vec{S}, \quad (1b)$$

$$\frac{d}{dt} \int_S \vec{B} \cdot d\vec{S} = - \oint_{\partial S} \vec{E} \cdot d\vec{l}, \quad (1c)$$

$$\frac{d}{dt} \int_V \rho \varepsilon dV = \int_V \vec{\sigma} : \nabla \vec{u} + \vec{j} \cdot \vec{E} dV, \quad (1d)$$

$$\frac{d}{dt} \int_V \frac{B^2}{2\mu_0} dV = \int_V \vec{\sigma}_B : \nabla \vec{u} - \frac{1}{\mu_0} \vec{B} \cdot \nabla \times \vec{E} dV, \quad (1e)$$

where the integration is performed over the volume V with the elements dV , (outward) oriented surface elements $d\vec{S}$ and oriented curve elements $d\vec{l}$. The permeability of free space μ_0 appears in the equations, since magnetic fields are considered to originate only from the free currents \vec{j} . They are purely solenoidal due to the assumed quasi-neutrality of the fluid, governed by the electrostatic Ampère's law $\vec{j} = 1/\mu_0 \nabla \times \vec{B}$. The model of resistive MHD then closes the system for the fluid-frame electric field \vec{E} by Ohm's law $\vec{E} = \eta \vec{j}$, where η is the electric resistivity. Note that also the Joule heating term $\vec{j} \cdot \vec{E}$ is included in the description, exchanging energy between the fluid and magnetic field. Finally, the closure relations determine the value

of the stress tensor $\bar{\sigma}$ as a function of the thermodynamic potentials and the symbol $\bar{\sigma}_B$ represents the magnetic stress tensor $\bar{\sigma}_B = 1/\mu_0(\vec{B} \otimes \vec{B} - 1/2\vec{B}^2\bar{I})$, where \bar{I} is the unit tensor.

The system of equations (1) reveals the fundamental conservation relations, which are respectively corresponding to the following quantities: mass, momentum, magnetic flux and internal energy. The additional equation for the magnetic energy (1e) can be seen as a consequence of Faraday's law and the Lorentz transformation of the laboratory-frame electric field \vec{E}' , which becomes $\vec{E} = \vec{E}' + \vec{u} \times \vec{B}$ in the non-relativistic limit ($|\vec{u}| \ll c$, where c is the speed of light). Therefore, this equation can be considered as an auxiliary part of the formulation, but it is essential for the construction of the energy-conserving numerical model as presented in section 3. Together, equations (1b), (1d) and (1e) yield conservation of the total energy on a Lipschitz domain Ω :

$$\begin{aligned} \int_{\Omega} \rho \varepsilon + \frac{B^2}{2\mu_0} + \frac{1}{2} \rho \vec{u}^2 dV &= \int_{\Omega} (\bar{\sigma} + \bar{\sigma}_B) : \nabla \vec{u} + \frac{1}{\mu_0} \nabla \times \vec{B} \cdot \vec{E} - \frac{1}{\mu_0} \vec{B} \cdot \nabla \times \vec{E} + \vec{u} \cdot \nabla \cdot (\bar{\sigma} + \bar{\sigma}_B) dV = \\ &= \oint_{\partial\Omega} \vec{u} \cdot (\bar{\sigma} + \bar{\sigma}_B) \cdot \vec{n} dS - \oint_{\partial\Omega} \frac{1}{\mu_0} \vec{E} \times \vec{B} \cdot d\vec{S} = 0. \end{aligned} \quad (2)$$

The last equality assumes the boundary conditions for zero Poynting vector and normal forces (\vec{n} is the outer normal) or a non-moving boundary.

For the numerical solution, the differential formulation is more suitable. The classical Reynolds transport theorem states for a field $\vec{A} = \vec{A}(t, \vec{x})$ on the domain $\Omega(t)$ moving with velocity \vec{v} :

$$\frac{d}{dt} \int_{\Omega(t)} \vec{A} dV = \int_{\Omega(t)} \frac{\partial}{\partial t} \vec{A} + (\vec{v} \nabla) \vec{A} + (\nabla \cdot \vec{v}) \vec{A} dV = \int_{\Omega(t)} \frac{d\vec{A}}{dt} + (\nabla \cdot \vec{v}) \vec{A} dV. \quad (3)$$

This formula can be generalized for (partially) solenoidal fields on the moving boundary of a surface $\Gamma(t)$ in the following way [22]:

$$\frac{d}{dt} \int_{\Gamma(t)} \vec{A} \cdot d\vec{S} = \int_{\Gamma(t)} \left(\frac{\partial}{\partial t} \vec{A} + (\nabla \cdot \vec{A}) \vec{v} + \nabla \times (\vec{A} \times \vec{v}) \right) \cdot d\vec{S} = \int_{\Gamma(t)} \frac{d\vec{A}}{dt} \cdot d\vec{S}. \quad (4)$$

Together with the gauge relation in the form of Gauss' law for the magnetic field $\nabla \cdot \vec{B} = 0$, this enables to rewrite the system (1) in the differential form for the Lagrangian frame:

$$\frac{d\rho}{dt} = -\rho \nabla \cdot \vec{u}, \quad (5a)$$

$$\rho \frac{d\vec{u}}{dt} = \nabla \cdot (\bar{\sigma} + \bar{\sigma}_B), \quad (5b)$$

$$\frac{d\vec{B}}{dt} = -\nabla \times \vec{E}, \quad (5c)$$

$$\rho \frac{d\varepsilon}{dt} = \bar{\sigma} : \nabla \vec{u} + \vec{j} \cdot \vec{E}, \quad (5d)$$

$$\rho \frac{d\varepsilon_B}{dt} = \bar{\sigma}_B : \nabla \vec{u} - \frac{1}{\mu_0} \vec{B} \cdot \nabla \times \vec{E}, \quad (5e)$$

where $\rho \varepsilon_B$ is the magnetic energy. This formulation assumes a full spatial dependency of the vector fields $\vec{E} = \vec{E}(t, \vec{x})$ and $\vec{B} = \vec{B}(t, \vec{x})$. However, the model is designed as multi-dimensional and it must be distinguished between the coplanar/collinear and transverse components in 1D and 2D. The reduced system in these lower dimensions is described in Appendix A.

3. Numerical model

The system of equations (5) together with the closure relations is solved numerically by the scheme described in this section. Its construction is based on the finite element method (FEM), which provides

flexibility in dimensionality of the problem, topology of the mesh and the choice of the polynomial orders of the discretization. The latter feature gives proportional convergence rates in turn, as shown in section 4. Moreover, the construction of the finite element spaces is consistent with the solved physical problem of section 2, satisfying the divergence-free constraint for the magnetic field and point-wise mass conservation by definition, as explained in the following subsections. The latter is related to the fact that curvilinear finite elements are used, which fit the Lagrangian framework and enable to track the motion of free boundaries and discontinuities in detail. However, the most appealing property of the new scheme is simultaneous conservation of all velocity moments, i.e, mass, momentum and energy for arbitrary orders of the elements.

3.1. Weak formulation

In order to derive a consistent finite element scheme, the considered system (5) is written in the variational form. The problem is formulated as mixed, where different functional spaces are used for approximation of the physical quantities. The three-dimensional model distinguishes the following spaces:

- thermodynamic (\mathcal{T}) – $\mathcal{T} \subset L_2(\Omega)$,
- kinematic (\mathcal{K}) – $\mathcal{K} \subset (H^1(\Omega))^3$,
- magnetic (\mathcal{M}) – $\mathcal{M} \subset H_{div}(\Omega)$,
- electric (\mathcal{E}) – $\mathcal{E} \subset H_{curl}(\Omega)$.

The solution of the system is then assumed to lay in the given spaces, specifically, $\vec{u} \in \mathcal{K}$, $\vec{B} \in \mathcal{M}$, $\vec{E} \in \mathcal{E}$ and $\varepsilon, \varepsilon_B \in \mathcal{T}$. Note that the density ρ is not included in the list, since it does not represent a primary variable here due to the geometric conservation law (GCL) for mass on curvilinear elements, as discussed in section 3.2. After multiplication by the test functions and imposing the smoothness requirements, the weak formulation of the system (5) (without the mass equation (5a)) together with Ohm's law can be obtained by integration:

$$\int_{\Omega} \rho \frac{d\vec{u}}{dt} \cdot \vec{\psi} dV = - \int_{\Omega} (\bar{\sigma} + \bar{\sigma}_B) : \nabla \vec{\psi} dV + \int_{\Gamma_{\sigma}} \bar{\sigma}_n \cdot \vec{\psi} dS, \quad \forall \vec{\psi} \in \mathcal{K}, \quad (6a)$$

$$\int_{\Omega} \frac{d\vec{B}}{dt} \cdot \vec{\Xi} dV = - \int_{\Omega} \nabla \times \vec{E} \cdot \vec{\Xi} dV, \quad \forall \vec{\Xi} \in \mathcal{M}, \quad (6b)$$

$$\int_{\Omega} \frac{1}{\eta} \vec{E} \cdot \vec{\xi} dV = \int_{\Omega} \frac{1}{\mu_0} \vec{B} \cdot \nabla \times \vec{\xi} dV - \int_{\Gamma_B} \frac{1}{\mu_0} \vec{B}^{\tau} \cdot \vec{\xi} dS, \quad \forall \vec{\xi} \in \mathcal{E}, \quad (6c)$$

$$\begin{aligned} \int_{\Omega} \rho \frac{d\varepsilon}{dt} \varphi dV &= \int_{\Omega} \bar{\sigma} : \nabla \vec{u} \varphi + \frac{1}{\mu_0} \vec{B} \cdot \nabla \times \vec{E} \varphi + \frac{1}{\mu_0} \vec{E} \times \vec{B} \cdot \nabla \varphi dV + \\ &+ \int_{\Gamma_E} \frac{1}{\mu_0} \vec{E}^{\tau} \cdot \mathbf{T} \vec{B} \mathbf{T} \varphi dS - \int_{\Gamma_B} \frac{1}{\mu_0} \vec{E} \cdot \vec{B}^{\tau} \mathbf{T} \varphi dS, \quad \forall \varphi \in \mathcal{T}, \quad (6d) \end{aligned}$$

$$\int_{\Omega} \rho \frac{d\varepsilon_B}{dt} \varphi dV = \int_{\Omega} \bar{\sigma}_B : \nabla \vec{u} \varphi - \frac{1}{\mu_0} \vec{B} \cdot \nabla \times \vec{E} \varphi dV, \quad \forall \varphi \in \mathcal{T}, \quad (6e)$$

where \mathbf{T} operator represents the trace of the functions on the boundary. A special treatment must be applied to the energy equations (6d) and (6e) to give them a mathematical sense. The integrals of products of three functions in $L_2(\Omega)$ may not converge in general and an additional constraint on uniform boundedness of φ can be imposed to cure the problem, as the functions are piece-wise polynomial in the discrete scheme of section 3.2 and the areas of the elements can be assumed as bounded too. Secondly, the gradient of φ is interpreted in the sense of generalized functions, where a finite number of removable discontinuities is present, on which the surface integrals can be evaluated. This is again motivated by the practical construction appearing in section 3.2 and the details can be found there. The formulation in the lower dimensions can be derived analogously and is presented in Appendix B alongside the choices of the functional spaces. However, the construction is consistent in all dimensions, maintaining identical overall properties.

The boundary conditions considered in (6) are the following:

$$\vec{u} = 0 \quad \text{on } \Gamma_u, \quad (\bar{\sigma} + \bar{\sigma}_B) \cdot \vec{n} = \bar{\sigma}_n \quad \text{on } \Gamma_\sigma, \quad \bar{\Gamma}_u \cup \bar{\Gamma}_\sigma = \partial\Omega, \quad \Gamma_u \cap \Gamma_\sigma = \emptyset, \quad (7a)$$

$$\vec{B} \times \vec{n} = \vec{B}^\tau \quad \text{on } \Gamma_B, \quad \vec{E} \times \vec{n} = \vec{E}^\tau \quad \text{on } \Gamma_E, \quad \bar{\Gamma}_B \cup \bar{\Gamma}_E = \partial\Omega, \quad \Gamma_B \cap \Gamma_E = \emptyset. \quad (7b)$$

The condition on Γ_u sets the non-moving (no-slip) boundary, Γ_σ prescribes the normal forces, Γ_B and Γ_E determine the tangential components of the magnetic and electric field, respectively. The boundary data are assumed to lay in L_2 on the corresponding boundary parts, while it is required that $\vec{E}^\tau \in C^1(\bar{\Gamma}_E)$ in order to be consistent with the definition of \mathcal{E} . It should be noted that the boundary conditions on Γ_u and Γ_E are essential, so they are imposed through the definitions of the corresponding spaces, which are consistent with them.

The choices of the functional spaces and the resulting weak form (6) reveal the essential aspects of the construction. Following the paradigm of the high-order curvilinear finite element hydrodynamics [18], the thermodynamic potentials are allowed to be discontinuous. This enables to maintain a sharp, non-oscillating solution across physical discontinuities like propagating shocks, for example. Furthermore, the weak formulation of the momentum equation introduces a symmetry between (6a) and the energy equations (6d) and (6e). This, in turn, leads to discrete conservation of kinetic energy, as shown in section 3.2. In addition, the weak form of Joule heating $\vec{j} \cdot \vec{E}$ provides symmetry between the energy equations (6d) and (6e), which yields conservation of discrete internal and magnetic energy. However, it is crucial to note that this term is still consistent with the strong Faraday's law (6b), so the correspondence between the magnetic field and the magnetic energy is preserved. Finally, the choice of the spaces \mathcal{M} and \mathcal{E} respects the natural transformation rules of the fields, i.e., constant normal magnetic flux and constant circulation of electric field [16]. This point becomes essential for the construction of the scheme on the curvilinear elements in section 3.2, where constant divergence of \vec{B} and curl of \vec{E} are maintained, despite the deformation. Moreover, the electrostatic Maxwell's equations (6b), (6c) follow the de Rham complex, which takes the following form in 3D [23]:

$$L_2 \xleftarrow{\nabla \cdot} H_{div} \xleftarrow{\nabla \times} H_{curl} \xleftarrow{\nabla} H^1. \quad (8)$$

Therefore, it holds $\nabla \times \vec{E} \in \mathcal{M}$ in Faraday's law (6b) exactly (for appropriately chosen spaces) and the divergence-free structure of \vec{B} is not affected, as $\nabla \cdot \nabla \times \vec{\xi} = 0$ for $\xi \in \mathcal{E}$ is exact too. Generally, the symmetric formulation of Maxwell's equations then provides a good conditioning of the discrete problem and consequently prevents locking of the solution [24].

Similar sequences exist in 2D, where the de Rham diagram becomes:

$$L_2 \xleftarrow{\nabla \cdot} H_{div} \xleftarrow{\nabla_{\parallel} \times} H^1, \quad L_2 \xleftarrow{\nabla_{\perp} \times} H_{curl} \xleftarrow{\nabla} H^1. \quad (9)$$

The operators for different components (coplanar and transverse) of the fields follow the notation of Appendix A. From the diagram, it is clear that the divergence-free structure of $\vec{B}_{\parallel} \in \mathcal{M}_{\parallel} \subset H_{div}(\Omega)$ is also maintained and the transformation of $\vec{E}_{\parallel} \in \mathcal{E}_{\parallel} \subset H_{curl}(\Omega)$ is physically consistent too, following the definition of the spaces in Appendix B.2.

In one dimension, the de Rham complex simplifies even further:

$$(L_2)^2 \xleftarrow{\nabla_{\perp} \times} (H^1)^2, \quad (10)$$

where it should be noted that the curl operator is a mere antisymmetric variation of gradient. Consequently, the 1D Faraday's law (B.1a) for $\vec{B}_{\perp} \in \mathcal{M}_{\perp} \subset (L_2)^2$ and $\vec{E}_{\perp} \in \mathcal{E}_{\perp} \subset (H^1)^2$ holds exactly too.

3.2. Semi-discrete model

Construction of the numerical scheme for solution of the weak formulation (6) continues with definitions of the finite element spaces and inference of a general discrete system in space, whereas the time discretization and specific choices of the functional bases are deferred to section 3.3.

In order to construct the spatial discretization on the curvilinear finite elements, the notion of the moving mesh must be defined:

$$\Omega(t) = \{\vec{x}(t, \vec{X}) \mid \vec{X} \in \Omega_0\}, \quad (11)$$

where $\vec{x}(t, \vec{X})$ is understood in this context as a time-dependent map relating the material coordinates $\vec{X} \in \Omega_0$ and the fluid element coordinates $\vec{x} \in \Omega(t)$. The material domain $\Omega_0 = \Omega(0)$ is taken as the initial one for simplicity, so it can be asserted $\vec{x}(0, \vec{X}) = \vec{X}$. The moving volume element coordinates $\vec{x}(t, \vec{X})$ follow the characteristics of the solution, being governed by the equation of motion $d\vec{x}/dt = \vec{u}$.

On the (static) Lipschitz domain Ω_0 , the tessellation Σ_h is considered, where the set of all internal edges is then denoted as Υ_h . A conforming discretization with the definitions in section 3.1 is made here, i.e., the finite dimensional subspaces $\mathcal{T}_h \subset \mathcal{T}, \mathcal{K}_h \subset \mathcal{K}, \mathcal{M}_h \subset \mathcal{M}, \mathcal{E}_h \subset \mathcal{E}$ are defined on Ω_0 . The base functions are then named as $\varphi_i \in \mathcal{T}_h$ for $i \in \{1, \dots, N_{\mathcal{T}}\}$, $\vec{\psi}_i \in \mathcal{K}_h$ for $i \in \{1, \dots, N_{\mathcal{K}}\}$, $\vec{\Xi}_i \in \mathcal{M}_h$ for $i \in \{1, \dots, N_{\mathcal{M}}\}$ and $\vec{\xi}_i \in \mathcal{E}_h$ for $i \in \{1, \dots, N_{\mathcal{E}}\}$. The primary variables are approximated by the grid functions designated in bold face as follows:

$$\vec{x}(t, \vec{X}) \approx \vec{x}_h(t, \vec{X}) = \sum_{i=1}^{N_{\mathcal{K}}} \mathbf{x}_i(t) \vec{\psi}_i(\vec{X}), \quad \vec{u}(t, \vec{X}) \approx \vec{u}_h(t, \vec{X}) = \sum_{i=1}^{N_{\mathcal{K}}} \mathbf{u}_i(t) \vec{\psi}_i(\vec{X}), \quad (12a)$$

$$\vec{B}(t, \vec{X}) \approx \vec{B}_h(t, \vec{X}) = \sum_{i=1}^{N_{\mathcal{M}}} \mathbf{B}_i(t) \vec{\Xi}_i(\vec{X}), \quad \vec{E}(t, \vec{X}) \approx \vec{E}_h(t, \vec{X}) = \sum_{i=1}^{N_{\mathcal{E}}} \mathbf{E}_i(t) \vec{\xi}_i(\vec{X}), \quad (12b)$$

$$\varepsilon(t, \vec{X}) \approx \varepsilon_h(t, \vec{X}) = \sum_{i=1}^{N_{\mathcal{T}}} \mathbf{e}_i(t) \varphi_i(\vec{X}), \quad \varepsilon_B(t, \vec{X}) \approx \varepsilon_{B_h}(t, \vec{X}) = \sum_{i=1}^{N_{\mathcal{T}}} \mathbf{e}_{B_i}(t) \varphi_i(\vec{X}). \quad (12c)$$

The definitions of the specific finite element spaces is deferred to section 3.3.5 to preserve generality of the construction, but it must be noted that they are piece-wise polynomial on the elements in all cases, satisfying $C^0(\overline{\Omega_e}) \cap C^1(\Omega_e)$ for the elements $\Omega_e \in \Sigma_h$. Following the Galerkin approach, the test functions are chosen from the identical spaces as the approximations of the primary variables (12). The resulting vectors, matrices and tensors after integration of the base functions over the domain $\Omega(t)$ are defined in Appendix C. The semi-discrete form of the physical system (5) is then obtained:

$$\frac{d\mathbf{x}}{dt} = \mathbf{u}, \quad (13a)$$

$$\mathbb{M}_{\mathcal{K}} \frac{d\mathbf{u}}{dt} = -(\mathbb{F} + \mathbb{F}_B) \mathbf{1} + \mathbf{b}_{\sigma}, \quad (13b)$$

$$\frac{d\mathbf{B}}{dt} = -\mathbb{C}_D \mathbf{E}, \quad (13c)$$

$$\mathbb{M}_{\mathcal{E}} \mathbf{E} = \frac{1}{\mu_0} \mathbb{C}_{jk} \mathbf{B}_j \mathbf{1}_k + \mathbb{X}_B^T \mathbf{1}, \quad (13d)$$

$$\mathbb{M}_{\mathcal{T}} \frac{d\mathbf{e}}{dt} = \mathbb{F}^T \mathbf{u} + \frac{1}{\mu_0} \mathbb{C}_{ij} \mathbf{E}_i \mathbf{B}_j + \mathbb{S}_{ij} \mathbf{E}_i \mathbf{B}_j + \mathbb{X}_E \mathbf{B} + \mathbb{X}_B \mathbf{E} + \mathbf{e}_B^c, \quad (13e)$$

$$\mathbb{M}_{\mathcal{T}} \frac{d\mathbf{e}_B}{dt} = \mathbb{F}_B^T \mathbf{u} - \frac{1}{\mu_0} \mathbb{C}_{ij} \mathbf{E}_i \mathbf{B}_j. \quad (13f)$$

Note that summation is performed over the repeated indexes and the dot index denotes the "free" index, where the vectorial notation is used. The vector $\mathbf{1}$ is the grid function corresponding to the unity in \mathcal{T}_h . The construction of the semi-discrete formulation in the lower dimensions (2D and 1D) is completely analogous, following the weak forms defined in Appendix B, and is not presented here for brevity.

3.2.1. Consistency properties

The semi-discrete Faraday's law (13c) utilizes the exact sequence given by the de Rham diagram (8), where $\nabla \times \vec{\xi} \in \mathcal{M}$ for $\vec{\xi} \in \mathcal{E}$. Similarly, the operator of the discrete curl $C_D : \mathcal{E}_h \mapsto \mathcal{M}_h$ can be defined together with its associated matrix \mathbb{C}_D [16]. Consequently, the following decomposition holds:

$$\mathbb{C}_{ijk} \mathbf{1}_k = (\mathbb{M}_{\mathcal{M}})_{jk} (\mathbb{C}_D)_{ki}. \quad (14)$$

Therefore, the mass matrix $\mathbb{M}_{\mathcal{M}}$ can be canceled on both sides of (6b) during the discretization procedure and (13c) is obtained. Thanks to this feature of the spaces, the mass matrix does not need to be inverted numerically, saving computational time and preventing numerical errors of an iterative solution to appear. Moreover, it is clear that functions $\nabla \cdot \vec{\Xi} \neq 0, \vec{\Xi} \in \mathcal{M}_h$ do not lie in range of C_D , so the divergence of \vec{B}_h remains constant. In order to guarantee this property even on the numerical level, an identical quadrature is used for numerical integration of $\mathbb{C} \cdot \mathbf{1}$ and $\mathbb{M}_{\mathcal{M}}$.

It is important to stress the consistency between the Faraday's law (13c) and the magnetic energy equation (13f) holds even on the semi-discrete level, even though the decomposition (14) is used. Without motion of the fluid ($\mathbf{u} = 0$), the change of the magnetic energy E_B is only due to the induced magnetic field:

$$\begin{aligned} \frac{d}{dt} E_B &= \frac{d}{dt} (\mathbf{1}^T \mathbb{M}_{\mathcal{T}} \mathbf{e}_B) = \mathbf{1}^T \mathbb{M}_{\mathcal{T}} \frac{d\mathbf{e}_B}{dt} = -\frac{1}{\mu_0} \mathbb{C}_{ijk} \mathbf{E}_i \mathbf{B}_j \mathbf{1}_k = \\ &= -\frac{1}{\mu_0} \mathbf{B}^T \mathbb{M}_{\mathcal{M}} \mathbb{C}_D \mathbf{E} = \frac{1}{\mu_0} \mathbf{B}^T \mathbb{M}_{\mathcal{M}} \frac{d\mathbf{B}}{dt} = \frac{d}{dt} \left(\frac{1}{2\mu_0} \mathbf{B}^T \mathbb{M}_{\mathcal{M}} \mathbf{B} \right), \end{aligned} \quad (15)$$

where symmetry of the mass matrices is used. When the fluid is in motion, the magnetic mass matrix $\mathbb{M}_{\mathcal{M}}$ is not constant, although $\mathbb{M}_{\mathcal{T}}$ is (see section 3.2.2). This change is due to mutual exchange of momentum between the fluid and magnetic field, but it is not captured perfectly by the transformation of the finite elements for the magnetic field (which are rather designed to conserve magnetic flux, see the next paragraph). Consequently, a marginal discrepancy between the left and right hand side of (15) arises, which is given by:

$$\mathbf{1}^T \mathbf{e}_B^c = \mathbf{1}^T \mathbb{F}_B^T \mathbf{u} - \frac{1}{2\mu_0} \mathbf{B}^T \frac{d\mathbb{M}_{\mathcal{M}}}{dt} \mathbf{B} \approx 0. \quad (16)$$

However, the correction term \mathbf{e}_B^c is evaluated and added to the right hand side of (13e) to conserve the total energy exactly, as proved in section 3.2.2. In this sense, consistency between the definitions of magnetic energy is recovered.

Finally, the transformation properties of the electric and magnetic finite elements naturally mimic the behavior of their physical counterparts. This feature becomes crucial when the computational mesh deforms, while physical consistency of \vec{E}_h and \vec{B}_h is retained without any necessary correction [16]. Specifically, magnetic flux and circulation of electric field are invariants of the transformation, which can be formulated differentially as:

$$\vec{B}_h \cdot \vec{n} dS = \frac{J}{|J|} \vec{B}'_h \cdot J^{-T} \vec{n}' |J| dS' = \vec{B}'_h \cdot \vec{n}' dS', \quad (17)$$

$$\vec{E}_h \cdot d\vec{l} = J^{-T} \vec{E}'_h \cdot J d\vec{l}' = \vec{E}'_h \cdot d\vec{l}', \quad (18)$$

where $J_{ij}(t, \vec{X}) = \partial \vec{x}_i / \partial \vec{X}_j(t, \vec{X})$ is the Jacobi matrix of the transformation from the material space (with quantities denoted by prime) to the fluid frame. Contravariant transformation is applied on the surface normal vector $\vec{n} = J^{-T} \vec{n}'$ and covariant on the curve element $d\vec{l} = J d\vec{l}'$. This proves that the Piola transformations $\vec{B}_h = |J|^{-1} J \vec{B}'_h$ and $\vec{E}_h = J^{-T} \vec{E}'_h$ satisfy the invariance when applied to the fields [25].

A similar situation appears in the lower dimensions and the Piola transformations are applied on the coplanar/collinear components of the fields. However, the transverse components must be considered too, despite the fact that the mesh deformation does not occur in this direction. The length of the normal vector \vec{n} and the curve element $d\vec{l}$ does not change, but the area of the surface element dS changes due to the deformation. Consequently, the transformations $\vec{B}_{\perp h} = |J|^{-1} \vec{B}'_{\perp h}$ and $\vec{E}_{\perp h} = \vec{E}'_{\perp h}$ must be applied onto the fields.

Furthermore, a non-uniform motion in the transverse direction also leads to the generation of magnetic fields, which is modeled by the $(\vec{B}_{\parallel} \nabla) \vec{u}_{\perp}$ term in (A.1b) and (A.2b). In order to write the equations for magnetic field (B.1a) and (B.2b) in a way similar to (13c), a discrete operator must be formulated for the term. The construction in 1D is straightforward, following the de Rham complex $L_2 \xleftarrow{\nabla} H^1$, which implies that $\nabla \vec{\psi}_{\perp} \in \mathcal{M}_{\perp}$ for $\vec{\psi}_{\perp} \in \mathcal{K}_{\perp}$ (for appropriately chosen spaces). As the functional spaces of \mathcal{M}_{\perp}

and \mathcal{M}_\parallel coincide in 1D up to the vector dimension (see Appendix B.1), the gradient can be point-wise weighted by \vec{B}_\parallel . In 2D, the de Rham diagram (9) yields $\nabla\vec{\psi}_\perp \in H_{curl}(\Omega_0) \subset (L_2(\Omega_0))^2$ for $\vec{\psi}_\perp \in \mathcal{K}_\perp$ and $\mathcal{M}_\parallel \subset H_{div}(\Omega_0) \subset (L_2(\Omega_0))^2$. The dot product is then performed point-wise in $(L_2(\Omega_0))^2$, obtaining the result in $\mathcal{M}_\perp \subset L_2(\Omega_0)$.

More formally, the projectors $\Pi_{\mathcal{M}_\parallel} : \mathcal{M}_\parallel \rightarrow \mathcal{M}_\perp^2$ and $\Pi_{\nabla\mathcal{K}_\perp} : \nabla\mathcal{K}_\perp \rightarrow \mathcal{M}_\perp^2$ must be constructed in 2D (and analogously in 1D). For simplicity, the identity operators are used for appropriately defined spaces, which result in point projection at the degrees-of-freedom of $\mathcal{M}_{\perp h}$ on the semi-discrete level. Afterwards, the dot contraction from $\mathcal{M}_\perp^2 \times \mathcal{M}_\perp^2$ to \mathcal{M}_\perp is performed point-wise, which is only exact for a (piece-wise) constant argument. Otherwise, a typically acceptable approximation error is introduced by the operation. However, note that only the transverse components are affected, which are not subjects of the divergence-free condition.

3.2.2. Conservation properties

Conservation properties are an essential part of the scheme design. A major role in the construction plays validity of the geometric conservation law (GCL), which can be written in the differential form as [26]:

$$\frac{d|J|}{dt} = |J|\nabla \cdot \vec{u}. \quad (19)$$

Since the functions from the kinematic space \mathcal{K}_h are differentiable, the Jacobi matrix J is consistently approximated as $J_h(t, \vec{X}) = \nabla_{\vec{X}} \vec{x}_h(t, \vec{X})$, where $\nabla_{\vec{X}}$ is the gradient w.r.t the material coordinates. From (13a), it can be deduced that GCL (19) holds discretely. For further details, see [18]. Consequently, the mass conservation law (5a) can be reformulated as $d\rho|J|/dt = 0$ and it holds point-wise on the discrete level for the density ρ_h defined as:

$$\rho_h(t, \vec{X}) = \rho_0(\vec{X})/|J_h(t, \vec{X})|, \quad (20)$$

where $\rho_0(\vec{X}) = \rho_h(0, \vec{X})$ is the initial profile of density. Note that the symbol ρ is favored in the rest of the work for better readability, but ρ_h is implied on the discrete level.

Another related feature of the scheme is the fact that the thermodynamic mass matrix $\mathbb{M}_{\mathcal{T}}$ and kinematic mass matrix $\mathbb{M}_{\mathcal{K}}$ are constant. Since the mapping follows the characteristics \vec{x}_h , material derivatives of the base functions $\{\varphi_i\}_{i=1}^{N_{\mathcal{T}}}$ and $\{\vec{\psi}_i\}_{i=1}^{N_{\mathcal{K}}}$ are zero (similarly for other base functions). The classical Reynolds theorem (3) together with the point-wise mass conservation and definitions of $\mathbb{M}_{\mathcal{T}}$ and $\mathbb{M}_{\mathcal{K}}$ (C.1) then implies the following:

$$\frac{d}{dt} (\mathbb{M}_{\mathcal{T}})_{ij} = \int_{\Omega(t)} \rho \left(\frac{d\varphi_i}{dt} \varphi_j + \varphi_i \frac{d\varphi_j}{dt} \right) dV = 0, \quad \frac{d}{dt} (\mathbb{M}_{\mathcal{K}})_{ij} = \int_{\Omega(t)} \rho \left(\frac{d\vec{\psi}_i}{dt} \cdot \vec{\psi}_j + \vec{\psi}_i \cdot \frac{d\vec{\psi}_j}{dt} \right) dV = 0. \quad (21)$$

Moreover, the absence of the inter-element constraints in the thermodynamic space $\mathcal{T}_h \subset L_2(\Omega_0)$ results in a block-diagonal structure of $\mathbb{M}_{\mathcal{T}}$. This means that the matrix can be inverted in each element separately without the need for a global iterative method.

Conservation of the total momentum P is an immediate consequence of (13b) and the definitions (C.3), which imply $(\mathbb{F}^T + \mathbb{F}_B^T)\mathbf{1}_{\mathcal{K}} = \mathbf{0}$. The vector $\mathbf{1}_{\mathcal{K}}$ is the grid function corresponding to the unit vector in \mathcal{K}_h and $\mathbf{0}$ is a zero vector of length $N_{\mathcal{T}}$. Provided that the boundary is not moving ($\Gamma_\sigma = \emptyset$) or the outer normal force is zero ($\sigma_n = 0$), conservation of momentum is proven as follows:

$$\frac{d}{dt} P = \frac{d}{dt} (\mathbf{1}_{\mathcal{K}}^T \mathbb{M}_{\mathcal{K}} \mathbf{u}) = \mathbf{1}_{\mathcal{K}}^T \mathbb{M}_{\mathcal{K}} \frac{d\mathbf{u}}{dt} = \mathbf{1}_{\mathcal{K}}^T (\mathbb{F} + \mathbb{F}_B) \mathbf{1} = 0, \quad (22)$$

where the fact that the mass matrix $\mathbb{M}_{\mathcal{K}}$ is constant is used.

The energy conservation property arises from the symmetries between the energy equations (13e), (13f) and the momentum equation (13b). Defining the discrete total energy E_T with help of the mass matrices,

the conservation can be proven:

$$\begin{aligned} \frac{d}{dt} E_T &= \frac{d}{dt} \left(\mathbf{1}^T \mathbb{M}_T \mathbf{e} + \mathbf{1}^T \mathbb{M}_T \mathbf{e}_B + \frac{1}{2} \mathbf{u}^T \mathbb{M}_K \mathbf{u} \right) = \left(\mathbf{1}^T \mathbb{M}_T \frac{d\mathbf{e}}{dt} + \mathbf{1}^T \mathbb{M}_T \frac{d\mathbf{e}_B}{dt} + \mathbf{u}^T \mathbb{M}_K \frac{d\mathbf{u}}{dt} \right) = \\ &= \mathbf{1}^T (\mathbb{F}^T + \mathbb{F}_B^T) \mathbf{u} - \mathbf{u}^T (\mathbb{F} + \mathbb{F}_B) \mathbf{1} + \mathbb{S}_{ijk} \mathbf{E}_i \mathbf{B}_j \mathbf{1}_k = 0, \end{aligned} \quad (23)$$

where symmetry and time-independence of the mass matrices \mathbb{M}_T , \mathbb{M}_K is used. In addition, the definition (C.7) of the tensor \mathbb{S} implies that $\mathbb{S} \cdot \mathbf{1} = \mathbb{O}_{\mathcal{E}\mathcal{M}}$, where $\mathbb{O}_{\mathcal{E}\mathcal{M}}$ is a zero matrix of size $N_{\mathcal{E}} \times N_{\mathcal{M}}$. It is also assumed that the Poynting vector across the boundary is equal to zero, so the boundary terms vanish.

3.3. Discrete model

The construction of the numerical scheme after formulation of the general semi-discrete system (13) proceeds with temporal and specific spatial discretization. The time integration is divided into two parts, magnetodynamic and ideally magneto-hydrodynamic. The magnetodynamic part described in section 3.3.1 is solved implicitly (due to its parabolic nature) on a static mesh, whereas the part representing ideal magneto-hydrodynamics is solved by the explicit scheme of section 3.3.2 (due to its hyperbolic nature) and the mesh position is advanced. The schemes are coupled together in a multi-step method described in section 3.3.3, which preserves the conservation properties of the scheme described in section 3.2.2.

3.3.1. Magnetodynamics

The magnetodynamic part of the scheme advances the discrete magnetic field \mathbf{B} and electric field \mathbf{E} without motion of the computational mesh. The time discretization is performed between the discrete time levels n and $n + 1$, which are designated by the upper index of the grid functions.

Within resistive MHD, eddy currents cause diffusion of the magnetic field and electric field consequently. Therefore, a (semi-)implicit time integration is desired for solution of the resulting parabolic system when the time step Δt is comparable with the diffusion time τ_B , i.e., $\Delta t \gtrsim \tau_B = \mu_0 L^2 / \eta$, where L is a characteristic length. However, the physical system might be nearly ideal ($\Delta t \ll \tau_B$) and an expensive implicit solution can be replaced by an explicit approach. For this reason, the parameter α is introduced to enable switching between the schemes:

$$\alpha = \begin{cases} 0 & \text{forward Euler (explicit, first order),} \\ 1/2 & \text{Crank-Nicolson (semi-implicit, second order, A-stable),} \\ 1 & \text{backward Euler (fully implicit, first order, L-stable).} \end{cases} \quad (24)$$

The magnetodynamic system, composed of the Faraday's law (13c) and Ohm's law (13d), is not solved in its primary mixed form, but transformed to an equation for the electric field by substitution of (13c) to (13d):

$$\left(\mathbb{M}_{\mathcal{E}} + \frac{\alpha}{\Delta t} \frac{1}{\mu_0} \mathbb{D} \right) \mathbf{E}^{n+1} = \frac{1}{\mu_0} \mathbb{C}_{.jk} \mathbf{B}_j^n \mathbf{1}_k - \frac{(1-\alpha)}{\Delta t} \frac{1}{\mu_0} \mathbb{D} \mathbf{E}^n + \mathbb{X}_B^T \mathbf{1}, \quad (25a)$$

$$\frac{1}{\Delta t} \mathbf{B}^{n+1} = \frac{1}{\Delta t} \mathbf{B}^n - \mathbb{C}_D \mathbf{E}^{n+\alpha}, \quad (25b)$$

where the electric field on the intermediate time level is interpolated as $\mathbf{E}^{n+\alpha} = \alpha \mathbf{E}^{n+1} + (1-\alpha) \mathbf{E}^n$. The newly appearing diffusion matrix \mathbb{D} is defined together with the rest of the matrices in Appendix C. However, it is consistent with the semi-discrete form and can be equivalently understood as the following composition of the matrices:

$$\mathbb{D}_{ij} = \mathbb{C}_{ikl} (\mathbb{C}_D)_{kj} \mathbf{1}_l. \quad (26)$$

This assertion can be viewed as a consequence of the compatibility of the spaces mentioned in section 3.2.1. After (25a) is solved numerically, the resulting electric field is inserted into (25b) to obtain the magnetic

field. This procedure guarantees that \mathbf{B}^{n+1} remains divergence-free even on the numerical level due to the properties of \mathbb{C}_D discussed in section 3.2.1.

When the new values of the fields are known, the explicit contribution to the energy equations (13e), (13f) can be evaluated:

$$\left. \frac{d\mathbf{e}}{dt} \right|_{\text{Joule}} = \mathbb{M}_{\mathcal{T}}^{-1} \left(+\frac{1}{\mu_0} \mathbb{C}_{ij} \cdot \mathbf{E}_i^{n+\alpha} \mathbf{B}_j^{n+1/2} + \mathbb{S}_{ij} \cdot \mathbf{E}_i^{n+\alpha} \mathbf{B}_j^{n+1/2} + \mathbb{X}_E \mathbf{B}^{n+1/2} + \mathbb{X}_B \mathbf{E}^{n+\alpha} \right), \quad (27a)$$

$$\left. \frac{d\mathbf{e}_B}{dt} \right|_{\text{Joule}} = \mathbb{M}_{\mathcal{T}}^{-1} \left(-\frac{1}{\mu_0} \mathbb{C}_{ij} \cdot \mathbf{E}_i^{n+\alpha} \mathbf{B}_j^{n+1/2} \right). \quad (27b)$$

It should be stressed that $\mathbb{M}_{\mathcal{T}}$ can be pre-inverted in an element-wise fashion, as mentioned in section 3.2.2. Therefore, (27) can be evaluated on the element level and the local update of the magnetic energy (27b) can be reused in (27a) due to the symmetry between the equations, so solution of the auxiliary equation for \mathbf{e}_B has nearly zero computational costs and preserves the symmetry numerically.

The choice of the time-centered magnetic field in (27) is motivated by the consistency with (25b), following the discussion of the semi-discrete form in section 3.2.1. When discretized this way, consistency of the magnetic field \mathbf{B} with the magnetic energy \mathbf{e}_B holds discretely:

$$\begin{aligned} (E_B^{n+1} - E_B^n) \Big|_{\text{Joule}} &= (\mathbf{1}^T \mathbb{M}_{\mathcal{T}} \mathbf{e}_B^{n+1} - \mathbf{1}^T \mathbb{M}_{\mathcal{T}} \mathbf{e}_B^n) \Big|_{\text{Joule}} = -\frac{\Delta t}{\mu_0} \mathbb{C}_{ijk} \mathbf{E}_i^{n+\alpha} \mathbf{B}_j^{n+1/2} \mathbf{1}_k = \\ &= \frac{1}{2\mu_0} ((\mathbf{B}^{n+1})^T - (\mathbf{B}^n)^T) \mathbb{M}_{\mathcal{M}} (\mathbf{B}^{n+1} + \mathbf{B}^n) = \frac{1}{2\mu_0} ((\mathbf{B}^{n+1})^T \mathbb{M}_{\mathcal{M}} \mathbf{B}^{n+1} - (\mathbf{B}^n)^T \mathbb{M}_{\mathcal{M}} \mathbf{B}^n), \end{aligned} \quad (28)$$

where symmetry of $\mathbb{M}_{\mathcal{M}}$ is used and zero boundary terms are assumed.

3.3.2. Ideal magneto-hydrodynamics

Unlike section 3.3.1, the part of the scheme dedicated to ideal magneto-hydrodynamics is solved explicitly and operates with an already known magnetic field, which enters the scheme only indirectly through the Lorentz force matrix \mathbb{F}_B . This part of the scheme, complementary to (25) and (27), is given by:

$$\left. \frac{d\mathbf{x}}{dt} \right|_{\text{hydro}} = \mathbf{u}^*, \quad (29a)$$

$$\left. \frac{d\mathbf{u}}{dt} \right|_{\text{hydro}} = -\mathbb{M}_{\mathcal{K}}^{-1} ((\mathbb{F} + \mathbb{F}_B) \mathbf{1} + \mathbf{b}_\sigma), \quad (29b)$$

$$\left. \frac{d\mathbf{e}}{dt} \right|_{\text{hydro}} = \mathbb{M}_{\mathcal{T}}^{-1} (\mathbb{F}^T \mathbf{u}^* + \mathbf{e}_B^c), \quad (29c)$$

$$\left. \frac{d\mathbf{e}_B}{dt} \right|_{\text{hydro}} = \mathbb{M}_{\mathcal{T}}^{-1} \mathbb{F}_B^T \mathbf{u}^*. \quad (29d)$$

The system is nearly identical to the original method of the high-order curvilinear finite element hydrodynamics [18] and is only augmented by addition of the Lorentz force $\mathbb{F}_B \mathbf{1}$ to the momentum equation (29b) and the equation for the magnetic energy (29d). The definition of the velocity \mathbf{u}^* varies depending on the time integration algorithm. For classical multi-step methods it is set equal to the starting (intermediate) time level, but time symmetry and energy conservation are lost this way. By contrast, the special choice of \mathbf{u}^* made in section 3.3.3 leads to fulfilling of the energy conservation. In all cases, momentum conservation is not affected by the choice of time stepping due to linearity of the expressions and the proof made for the semi-discrete form in section 3.2.2 holds discretely too.

3.3.3. Time integration

The time discretization of the coupled system (25), (27) and (29) can follow different strategies depending on the coupling of the system, which is approximately characterized by the magnetic Reynolds number

$\text{Re}_m = uL\mu_0/\eta$. In cases dominated by diffusion ($\text{Re}_m \ll 1$) or by convection ($\text{Re}_m \gg 1$), operator splitting can be applied to the system and an arbitrarily high order of the time integration scheme can be used for the explicit hydrodynamic part (29). For this purpose, energy-conserving implicit-explicit (IMEX) methods are used [27]. A special case is the second order RK2-Average scheme, which allows to combine the magnetodynamics and ideal magneto-hydrodynamics. The improved inter-coupling between the two parts favours this method in the case of a strong coupling ($\text{Re}_m \sim 1$).

Within the high-order conservative IMEX methods, the vector of the state variables is split into implicit and explicit parts. The implicit part V is dedicated to velocity and conserves kinetic energy due to its symplectic nature. The explicit part Y accommodates the rest of the quantities:

$$V = [\mathbf{u}], \quad Y = [\mathbf{x}, \mathbf{e}, \mathbf{e}_B]^T. \quad (30)$$

In the case of the lower-dimensional formulations, the hydrodynamic update of the magnetic field is included in the state Y . The calculation uses the derivatives $V' = V'(t, Y)$ and $Y' = Y'(t, V, Y)$ given by (29) with the Butcher tables, which can be found for the third (RK3hc) and fourth order schemes (RK4hc) in [27]. However, it must be stressed that the lower-triangular form of the Butcher tables for the selected class of implicit methods together with the only dependency of V' on the explicit state Y allows to solve the velocity equation (29b) explicitly.

A special case of the IMEX methods is the RK2-Average scheme used for the high-order curvilinear finite element hydrodynamics [18], but extended for the Lorentz force contribution to the momentum equation (29b) and the Joule heating terms (27). It can be derived from the classical RK2 method, sharing with it the second order of convergence. The first step of the method calculates the quantities on the intermediate time level $n + 1/2$ as follows:

$$\mathbf{u}^{n+1/2} = \mathbf{u}^n - \frac{\Delta t}{2} \mathbb{M}_{\mathcal{K}}^{-1} ((\mathbb{F}^n + \mathbb{F}_B^n) \mathbf{1} + \mathbf{b}_\sigma^n), \quad (31a)$$

$$\mathbf{x}^{n+1/2} = \mathbf{x}^n + \frac{\Delta t}{2} \mathbf{u}^{n+1/2}, \quad (31b)$$

$$\mathbf{e}^{n+1/2} = \mathbf{e}^n + \frac{\Delta t}{2} \mathbb{M}_{\mathcal{T}}^{-1} (\mathbb{F}^n)^T \mathbf{u}^{n+1/2} + \frac{\Delta t}{2} \left. \frac{d\mathbf{e}}{dt} \right|_{\text{Joule}}^{n, \Delta t/2}, \quad (31c)$$

$$\mathbf{e}_B^{n+1/2} = \mathbf{e}_B^n + \frac{\Delta t}{2} \mathbb{M}_{\mathcal{T}}^{-1} (\mathbb{F}_B^n)^T \mathbf{u}^{n+1/2} + \frac{\Delta t}{2} \left. \frac{d\mathbf{e}_B}{dt} \right|_{\text{Joule}}^{n, \Delta t/2}, \quad (31d)$$

where the superscript of the Joule heating terms defined by (27) denotes the time level for construction of the matrices and length of the time step, respectively. The second step of the method takes the following form:

$$\mathbf{u}^{n+1} = \mathbf{u}^n - \Delta t \mathbb{M}_{\mathcal{K}}^{-1} ((\mathbb{F}^{n+1/2} + \mathbb{F}_B^{n+1/2}) \mathbf{1} + \mathbf{b}_\sigma^{n+1/2}), \quad (32a)$$

$$\mathbf{x}^{n+1} = \mathbf{x}^n + \Delta t \bar{\mathbf{u}}^{n+1/2}, \quad (32b)$$

$$\mathbf{e}^{n+1} = \mathbf{e}^n + \Delta t \mathbb{M}_{\mathcal{T}}^{-1} (\mathbb{F}^{n+1/2})^T \bar{\mathbf{u}}^{n+1/2} + \Delta t \left. \frac{d\mathbf{e}}{dt} \right|_{\text{Joule}}^{n+1/2, \Delta t} + \mathbf{e}_B^c, \quad (32c)$$

$$\mathbf{e}_B^{n+1} = \mathbf{e}_B^n + \Delta t \mathbb{M}_{\mathcal{T}}^{-1} (\mathbb{F}_B^{n+1/2})^T \bar{\mathbf{u}}^{n+1/2} + \Delta t \left. \frac{d\mathbf{e}_B}{dt} \right|_{\text{Joule}}^{n+1/2, \Delta t}, \quad (32d)$$

where the intermediate velocity is defined as $\bar{\mathbf{u}}^{n+1/2} = 1/2(\mathbf{u}^{n+1} + \mathbf{u}^n)$. The correction term \mathbf{e}_B^c is calculated between the time levels n and $n + 1$.

As mentioned already, the RK2-Average scheme conserves the total energy E_T . Following the lines of the proof in section 3.2.2 for the semi-discrete form, the conservation can be proven:

$$\begin{aligned} E_T^{n+1} - E_T^n &= \left(\mathbf{1}^T \mathbb{M}_{\mathcal{T}} (\mathbf{e}^{n+1} + \mathbf{e}_B^{n+1} - \mathbf{e}^n - \mathbf{e}_B^n) + (\mathbf{u}^{n+1})^T \mathbb{M}_{\mathcal{K}} \mathbf{u}^{n+1} - (\mathbf{u}^n)^T \mathbb{M}_{\mathcal{K}} \mathbf{u}^n \right) = \\ &= \mathbf{1}^T ((\mathbb{F}^{n+1/2})^T + (\mathbb{F}_B^{n+1/2})^T) \bar{\mathbf{u}}^{n+1/2} - (\bar{\mathbf{u}}^{n+1/2})^T (\mathbb{F}^{n+1/2} + \mathbb{F}_B^{n+1/2}) \mathbf{1} + \mathbb{S}_{ijk} \mathbf{E}_i^{n+1/2} \mathbf{B}_j^{n+1/2} \mathbf{1}_k = 0. \end{aligned} \quad (33)$$

The time step control adopts the algorithm of the high-order curvilinear finite element hydrodynamics, where a CFL (Courant–Friedrichs–Lewy) criterion is based on the minimal singular value of J_h at the integration points [18]. In order to account for the magnetic stress contribution, the condition is modified in that the speed of sound c_s is replaced by the magneto-sonic velocity $v_f^2 = c_s^2 + v_A^2$, where $v_A = |\vec{B}|/\sqrt{\mu_0\rho}$ is the Alfvén velocity. The characteristics with slope equal to v_f represent the fastest propagating modes in classical MHD [28], guaranteeing stability for the scheme in turn.

3.3.4. Artificial viscosity

For stabilisation of the numerical scheme, artificial viscosity is used similarly to the high-order curvilinear hydrodynamics [18]. Its role is to transform kinetic energy to internal at places of strong compression to prevent oscillatory behaviour and deterioration of the mesh [29]. The artificial viscosity enters the numerical scheme through the definition of the stress tensor $\vec{\sigma} = -p\vec{I} + \vec{\sigma}_a$, where p is thermodynamic pressure and $\vec{\sigma}_a$ is the artificial viscosity tensor. The physical part of the tensor is simplified to the isotropic pressure only for all cases considered here, but the method is general and a non-artificial viscosity can be present. Multiple methods for construction of $\vec{\sigma}_a$ were proposed in [18, 30] and are not repeated here for brevity, but all of them rely on the tensor $\nabla\vec{u}_\parallel$. The multi-dimensional formulation of the viscosity is used here to take into account the transverse components of the velocity \vec{u}_\perp in the lower dimensions. The gradient $\nabla\vec{u}$ is calculated and complemented to a square tensor by zeros, assuming that the transverse derivatives vanish for the slab geometry. The rest of the procedure is identical with the original method and is performed in the plane/line. The only exception is the modification of the characteristic velocity in the CFL condition, where the magneto-sonic waves velocity v_f replaces the sound speed velocity, analogously to section 3.3.3.

3.3.5. Specific spatial discretization

The section about semi-discrete form (section 3.2) already defined the finite element spaces for the spatial discretization, but only in a general manner, with respect to their conformity with the functional spaces. The generality of the description allows to use various finite element families for different geometries on unstructured meshes. However, the numerical tests of section 4 narrow the scope of the practical verification of numerical properties to only regular hexahedral meshes with the following finite element spaces equipped with an isoparametric mapping:

- thermodynamic – $\mathcal{T}_h = \{\varphi \in \mathcal{T} \mid \varphi|_{\Omega_e} \in C^p(\Omega_e) \quad \forall \Omega_e \in \Sigma_h\}$,
- kinematic – $\mathcal{K}_h = \{\vec{\psi} \in \mathcal{K} \mid \vec{\psi}|_{\Omega_e} \in (C^{p+1}(\Omega_e))^3, \vec{\psi}|_{\Gamma_e} \in (Q^{p+1}(\Omega_e))^3 \quad \forall \Omega_e \in \Sigma_h, \Gamma_e \subset \partial\Omega_e\}$,
- magnetic – $\mathcal{M}_h = \{\vec{\Xi} \in \mathcal{M} \mid \vec{\Xi}|_{\Omega_e} \in RT_{3D}^{q+1}(\Omega_e) \quad \forall \Omega_e \in \Sigma_h\}$,
- electric – $\mathcal{E}_h = \{\vec{\xi} \in \mathcal{E} \mid \vec{\xi}|_{\Omega_e} \in ND_{3D}^{q+1}(\Omega_e) \quad \forall \Omega_e \in \Sigma_h\}$,

where C^p and Q^p are products of polynomials up to the order p in 3D and 2D, respectively. The sets Γ_e represent the faces of the element Ω_e . The polynomial spaces RT_{3D}^p and ND_{3D}^p represent the Nédélec H_{div} and H_{curl} conforming spaces in 3D, respectively [31], having the maximal polynomial order p . The construction in the lower dimensions is analogous and left for Appendix D.

Despite the fact that the construction of the semi-discrete model in section 3.2 does not require it, the polynomial orders are derived from only the parameters p and q for optimal conditioning. The orders in the hydrodynamic part are related through the term $\mathbb{F}^T\mathbf{u}$, where the kinematic elements with the polynomial order higher by one are optimal for regularization of the energy equation (13e), as the velocity is differentiated. The orders in the electromagnetic part are identical, because of the compatibility between the spaces, as explained in section 3.2.1. Henceforth, the elements of this kind are denoted as $TpMq$. The lowest order $T0M0$ elements are depicted in Figure 1.

Finally, it must be noted that the classical Lagrange elements are used for the kinematic quantities from \mathcal{K}_h , but Bernstein polynomials are preferred for the thermodynamic space \mathcal{T}_h . This choice is motivated by positivity of the approximated physical quantities, that is specific internal energy and specific magnetic

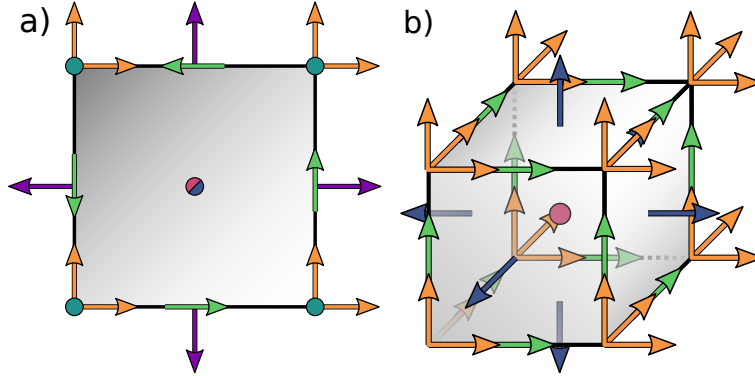


Figure 1: The magneto-hydrodynamic finite elements $TOM0$ in 2D (a) and 3D (b). The colors represent different degrees-of-freedom: **red** – thermodynamic, **orange** – kinematic, **blue** – (transverse) magnetic field, **green** – (coplanar) electric field, **purple** – coplanar magnetic field (only (a)), **cyan** – transverse electric field (only (a)).

energy. Since these polynomials form a positive basis, the interpolated functions are always positive when the discrete values of the corresponding grid functions are. Consequently, the mass matrices $\mathbb{M}_{\mathcal{T}}$ are positive definite. From the practical point of view, this feature prevents overshoots of the thermodynamic potentials near discontinuities like propagating shocks, for example [32].

4. Numerical tests

A series of tests was performed to validate construction of the proposed scheme and assess its performance. Propagation of magneto-hydrodynamic waves is examined in section 4.1. Convergence is measured on the smooth problems of ideal magneto-hydrodynamics in section 4.2 and resistive magnetodynamics in section 4.3. Furthermore, section 4.4 and section 4.5 show the capabilities of the scheme in 2D and 3D on physically relevant problems.

The numerical implementation utilizes the MFEM library for assembly of the finite elements, providing flexibility and scalability [33, 34]. The visualizations were made with the GLVis tool for fast and accurate rendering of high order finite elements [35].

4.1. MHD waves

The first test problem mainly concentrates on validation of the numerical scheme by the problem of MHD waves propagation. In contrast to the rest of the test cases, the problem is defined in one dimension, but both, colinear and transverse, components of the fields are involved.

The problem is adopted from [28] and is defined as a Riemann problem with the following left and right states:

$$\begin{pmatrix} \rho_l \\ \vec{u}_l \\ p_l \\ (\vec{B}_l)_x \\ (\vec{B}_l)_y \\ (\vec{B}_l)_z \end{pmatrix} = \begin{pmatrix} 3 \\ \vec{0} \\ 3 \\ 1.5 \\ 1 \\ 0 \end{pmatrix}, \quad \begin{pmatrix} \rho_r \\ \vec{u}_r \\ p_r \\ (\vec{B}_r)_x \\ (\vec{B}_r)_y \\ (\vec{B}_r)_z \end{pmatrix} = \begin{pmatrix} 1 \\ \vec{0} \\ 1 \\ 1.5 \\ \cos(\chi) \\ \sin(\chi) \end{pmatrix}. \quad (34)$$

Note that the values are given in relative units, where the magnetic field is normalized by $\sqrt{\mu_0}$. The twist angle of magnetic field is set to $\chi = 1.5$, which is close enough to $\pi/2$ to seed a large variety of magneto-hydrodynamic waves [28]. A solution is sought on the domain $(-1, 1)$, where the interface is located at the origin of the coordinate system. The boundary conditions for zero velocity are applied in agreement with the initial conditions.

The numerical solution is computed up to the final time 0.4 with different orders of the finite elements. The time integration scheme RK2-Average is used for $T0M0$ and $T1M1$ elements, RK3hc(A. α) for $T2M2$ and RK4hc(A. α) for $T3M3$ (consult section 3.3.3). In all cases, the CFL constant is set to 0.5. As the problem involves propagating discontinuities, it is sensitive to the choice of the artificial viscosity model. The best results were obtained with the model based on a full eigenvector decomposition of the velocity gradient [18, 30], which is also used in the following sections. Its linear coefficient is set to the value 0.25 and the quadratic to 1. The resolution keeps a constant number of degrees-of-freedom (DOFs) to give comparable results. Specifically, the mesh consists of 480 $T0M0$, 240 $T1M1$, 160 $T2M2$ or 120 $T3M3$ elements.

The results of the simulations are presented in Figure 2 together with the analytic solution [28, 36]. As already mentioned, the solution involves multiple linear waves. Going from the left, it is a fast rarefaction wave, rotational Alfvénic wave, slow rarefaction wave, contact discontinuity, slow shock wave, rotational Alfvénic wave and fast shock wave. Note that not all waves appear in all figures. For example, the rotational waves are not associated with any normal compression and thus they are only visible in the plots of the transverse velocity and magnetic field. To summarize the results, the curves for all finite elements except the piece-wise constant $T0M0$ are nearly identical. This can be seen as an implication of the Lax theorem limiting the convergence to the first order only at discontinuities. However, it is important that precision is not lost for higher order elements, even though their amount is lower. The zeroth order elements exhibit small over/undershoots near the rotational waves mainly. This phenomenon can be probably attributed to the staggered-like discretization of the transverse magnetic field and velocity according to Appendix B.1. A slight difference between the elements of different orders can be recognized at the head of the fast rarefaction wave (around $x \approx -0.6$), where the solution is continuous. As can be expected, the overshoot decreases with an increasing order of the elements. On the other hand, the so-called wall heating effect near the contact discontinuity (around $x \approx 0.15$) is slightly stronger for the higher order elements. This effect originates from the beginning of the simulation, when artificial viscosity was very active and the higher order elements naturally tended to oscillate more strongly due to Runge’s phenomenon.

4.2. MHD Taylor-Green vortex

In order to assess convergence of the scheme, the classical steady-state solution of incompressible, inviscid Navier–Stokes equations known as the Taylor-Green vortex was extended to the coplanar ideal MHD. The magnetic field is specifically chosen as $\vec{B} = \beta\sqrt{\mu_0}\vec{u}$ with β being an arbitrary constant, which automatically guarantees divergence-free structure of the field. The stationary solution is then given by the equations:

$$\vec{u}_x(x, y) = \sin(\pi x) \cos(\pi y), \quad (35a)$$

$$\vec{u}_y(x, y) = -\cos(\pi x) \sin(\pi y), \quad (35b)$$

$$p(x, y) = 1 + \frac{1 - \beta^2}{4}(\cos(2\pi x) + \cos(2\pi y)) - \frac{\beta^2}{2}(\sin^2(\pi x) \cos^2(\pi y) + \cos^2(\pi x) \sin^2(\pi y)). \quad (35c)$$

Note that unlike the classical formulation for plain hydrodynamics [18], the second term appears in (35c) to compensate for the magnetic pressure.

Following the methodology of [18], the solution is extended to the compressible (magneto-)hydrodynamics by means of the method of manufactured solution. In essence, the following energy source term is added to the energy equation to compensate for the mechanical work:

$$S_e = \frac{3}{8}\pi(\cos(3\pi x) \cos(\pi y) - \cos(\pi x) \cos(3\pi y)). \quad (36)$$

The equation of ideal gas is considered here with the Poisson constant $\gamma = 5/3$, atomic weight $A = 1$ and proton number $Z = 1$. The density profile is homogeneous with $\rho \equiv 1$. The problem is solved on a unit square with the boundary conditions for zero velocities.

The numerical solution at the final time $t = 0.75$ (in relative units) is plotted in Figure 3, where the computational mesh has 20 quadratic/cubic T2M2 finite elements in each dimension. The factor of the magnetic field is set to $\beta = 0.5$, corresponding to the ratio 4:1 between the dynamic and magnetic pressure.

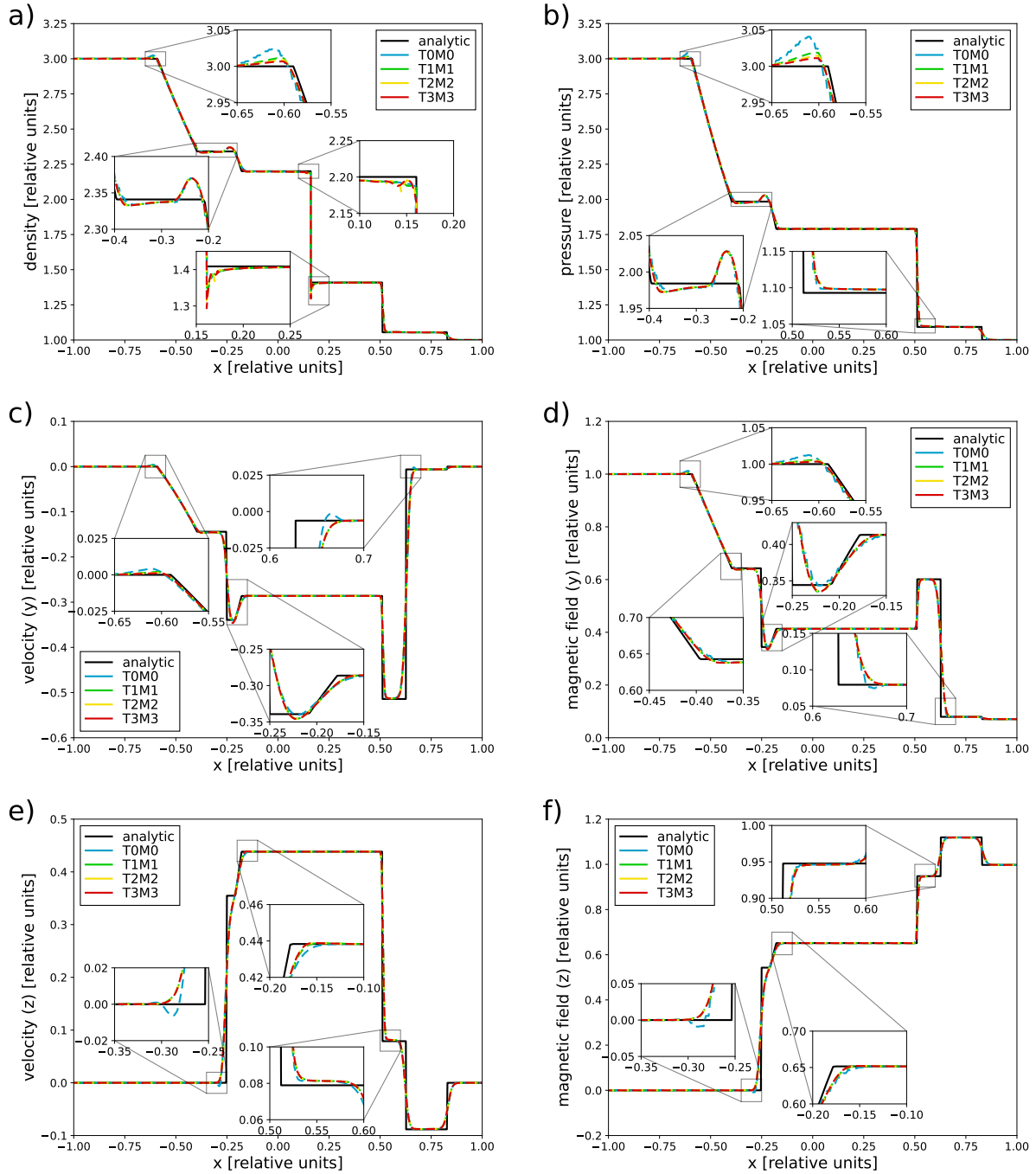


Figure 2: Numerical solution of the MHD wave problem: a) density b) pressure c) velocity (y component) d) magnetic field (y component) e) velocity (z component) f) magnetic field (z component). The legend denotes the finite elements used. See the accompanying text for details.

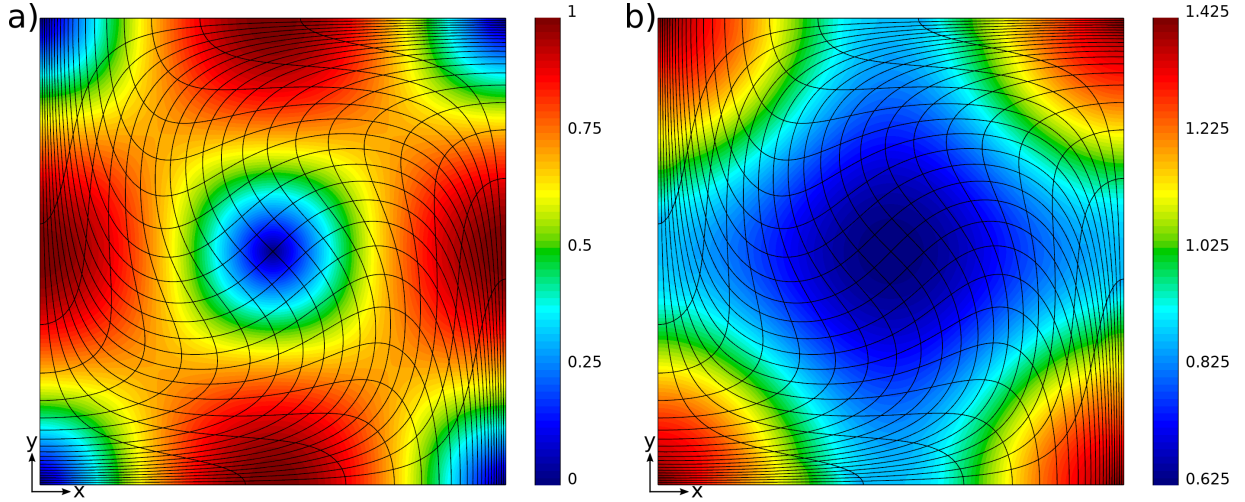


Figure 3: Numerical solution of the magneto-hydrodynamic Taylor-Green vortex problem with $\beta = 0.5$ at the final time $t = 0.75$: a) magnitude of velocity [relative units] b) pressure [relative units]. The computational mesh has 20×20 finite elements of the $T2M2$ family.

The time integration used RK3hc(A. α) scheme with the CFL factor 0.5 (see section 3.3.3). From the results, the deformation of the curvilinear finite elements due to the mass flow is apparent, but the sufficiently high order of interpolation preserves a good accuracy of the solution without any significant imprints of the mesh.

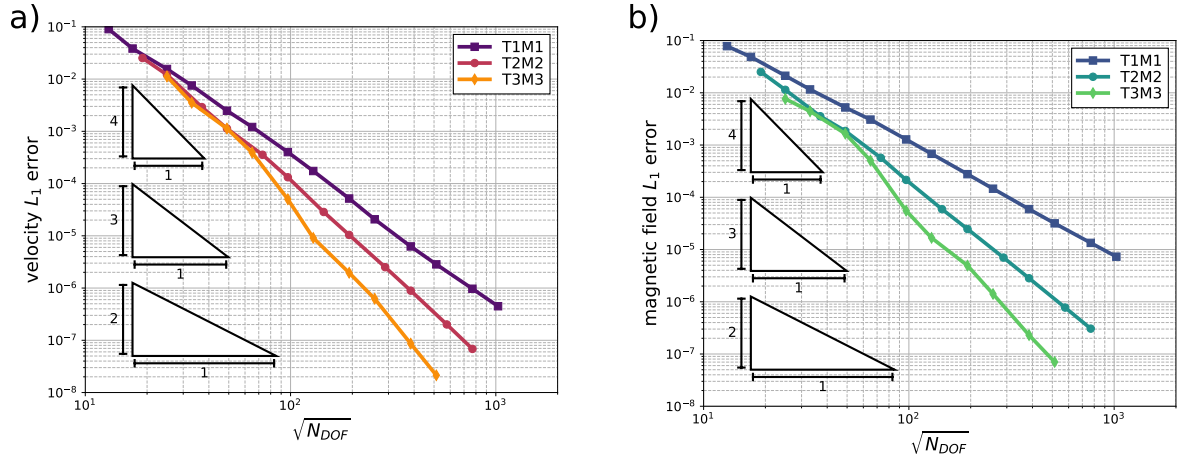


Figure 4: Dependencies of the velocity (a) and magnetic field (b) L_1 integral error on the number of degrees-of-freedom for the magneto-hydrodynamic Taylor-Green vortex problem with $\beta = 0.5$ at the final time $t = 0.75$. The finite elements used are denoted in the legend.

Resilience of the curvilinear finite elements to mesh deformation is also confirmed by the convergence plots in Figure 4 for varying number degrees-of-freedom (and the time step due to the applied CFL condition). In particular, the symbol N_{DOF} designates the number of degrees-of-freedom for the H^1 -conforming basis, which can be related to the number of elements along each axis N_x, N_y through $N_{DOF} = ((p+1)N_x + 1)((p+1)N_y + 1)$ for $TpMp$ elements. The time integration schemes are chosen to match the spatial order of elements, where RK2-Average, RK3hc(A. α) and RK4hc(A. α) are used used for $T1M1, T2M2$ and $T3M3$ elements respectively (see section 3.3.3). The plots clearly indicate convergence rates with the order at least proportional to the order of the thermodynamic/magnetic basis. Moreover, the velocities exceed this rate with the average slope approximately 2.76 for $T1M1$, 3.48 for $T2M2$ and 4.29 for $T3M3$ elements.

This points to the fact that the magnetic pressure contributes to the momentum equation (5b) unlike the classical problem ($\beta = 0$). The order of the magnetic pressure term then surpasses that of the thermal pressure. When the magnetic contribution is not negligible compared the thermal ($\beta \gtrsim 1$), the velocity can benefit from this increase due to its higher by one interpolation order compared to the thermodynamic basis (see the definitions in section 3.3.5). Therefore, the resulting order of convergence ranges between the thermodynamic and kinematic orders of interpolation, where the increase diminishes for higher orders of elements and low values of the β parameter.

4.3. Magnetic diffusion

Following the previous section, convergence of the proposed numerical scheme is evaluated, but rather the magnetodynamic part is investigated in this case. An initial profile of magnetic field $\vec{B}(\vec{x}) = \delta\vec{B}\sqrt{\mu_0}\exp(-|\vec{x}|^2/\sigma_0^2)$ is considered, which is being diffused by means of resistive eddy currents, while the rest of the quantities is constant initially. Despite the fact that the problem is not fully physically realistic, as the magnetic field forms a magnetic monopole, the divergence is conserved (see section 3.2.1) and the problem has a simple analytic solution asymptotically:

$$\vec{E} = \frac{\eta}{\mu_0}\nabla \times \vec{B}, \quad \frac{\partial \vec{B}}{\partial t} = -\nabla \times \vec{E} = \frac{\eta}{\mu_0}(\Delta\vec{B} - \nabla(\nabla \cdot \vec{B})), \quad (37)$$

$$\vec{B}(t, \vec{x}) = \delta\vec{B}_0\sqrt{\mu_0} \left(\frac{\sigma_B}{\sigma(t)}\right)^{3/2} \exp\left(-\frac{|\vec{x}|^2}{\sigma(t)^2}\right), \quad \sigma(t) = \sqrt{\sigma_0^2 + 4\eta t/\mu_0}. \quad (38)$$

It can be noticed that the divergence contributes to the solution according to (37), but only through higher orders of the expansion in $\eta_m t/\sigma_0^2$, where $\eta_m = \eta/\mu_0$ is the magnetic diffusivity. Therefore, these terms can be truncated for a sufficiently small ratio. Furthermore, the magnetic Reynolds number $R_m = u\sigma_0/\eta_m$ must be kept small to prevent convection of the field, but the velocity can be approximated from the momentum equation giving $R_m \sim t|\delta\vec{B}|^2/\eta_m$. Finally, the effect of Joule heating must be suppressed, which is proportional to $t/\eta E^2 \sim t\eta_m|\delta\vec{B}|^2/\sigma_0^2$. However, when compared to the magnetic pressure $|\delta\vec{B}|^2/2$, the factor $\eta_m t/\sigma_0^2$ is obtained again.

4.3.1. Convergence analysis

The asymptotic problem is solved on the domain $(-1, 1)^d$, where d is the dimension. The width of the profile is $\sigma_0 = 0.1$ to avoid boundary effects, since the boundary condition on zero tangential magnetic field is applied. The diffusivity is set to $\eta_m = 1$ and the magnetic field $\delta\vec{B} = (1, 1, 1)$. To satisfy the stated criteria, the final time is only as short as $t = 10^{-10}$. Since the problem is asymptotic, only a single step of the simulation is performed with the *RK1* method for the hydrodynamic part and the backward Euler scheme for the magnetodynamic part (see section 3.3.1), which eliminates the dependency on the initial electric field due to its fully implicit nature.

Convergence of the electric field in 2D is plotted in Figure 5 for different finite elements. The results show a clear proportionality of the order of convergence to the polynomial order of the electric field elements $p + 1$ for *TpMp* elements. An exception from the rule is posed by the *T0M0* element in the out-of-plane component. In this configuration, the solution for the electric field benefits from the staggered-like discretization (see section 3.3.5) and converges with the second order. However, the effect is not propagated to convergence of the coplanar magnetic field, which has an insufficient order of the elements and converges only with the first order (not shown).

The results for the 3D case are presented in Figure 6. The trends closely resemble the coplanar electric field in 2D, where the order of convergence is given by the polynomial order of the electric field elements. The increased convergence rate observed for the out-of-plane component in 2D is not replicated here.

4.3.2. Energy conservation

In addition to the asymptotic convergence analysis, an elucidating insight is obtained from the non-asymptotic case, where conservation of energy can be studied. The parameters are kept identical, but

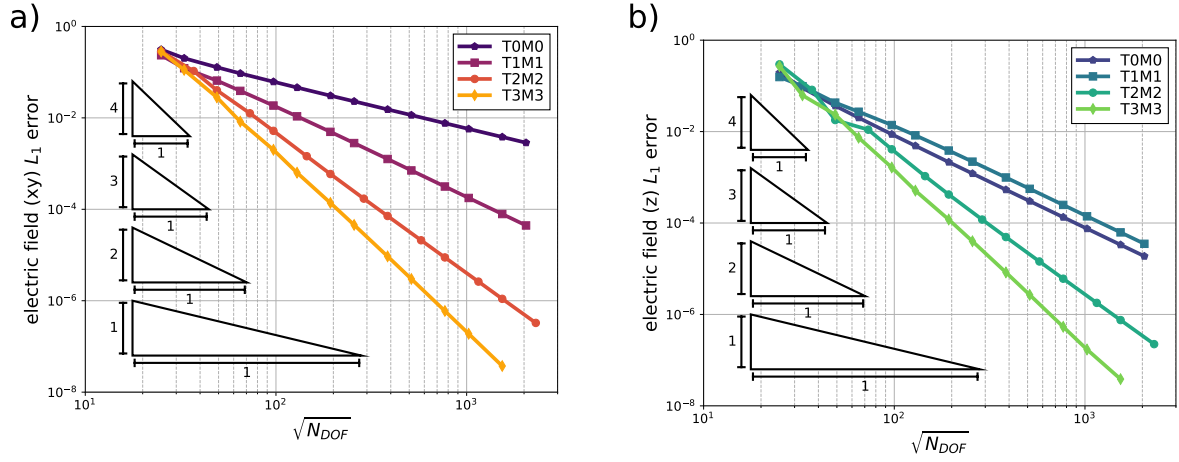


Figure 5: Electric field in xy -plane (a) and z -axis (b) L_1 error dependencies on the number of degrees-of-freedom for the magnetic diffusion problem in 2D. The asymptotic setting of the problem is considered with the final time $t = 10^{-10}$. The finite elements used are denoted in the legend.

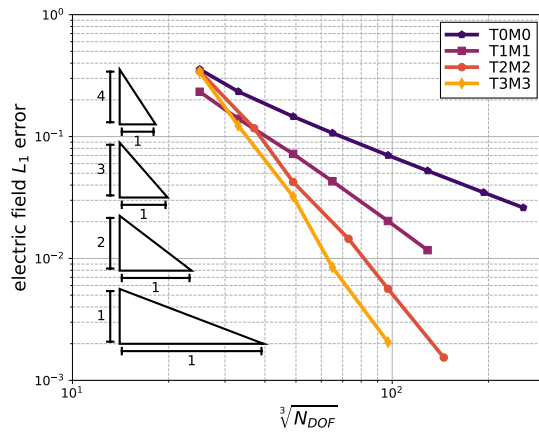


Figure 6: Electric field L_1 error dependencies on the number of degrees-of-freedom for the magnetic diffusion problem in 3D. The asymptotic setting of the problem is considered with the final time $t = 10^{-10}$. The finite elements used are denoted in the legend.

the final time is increased to $t = 0.02$. Moreover, the width of the initial Gaussian profile is increased to $\sigma_0 = 0.3$, as the boundary effects do not contribute to the energy balance and the boundary conditions can be tested this way. Unlike the previous case, where internal energy of the homogeneous medium did not play a role, it becomes essential for evaluation of the energy exchange process and it is set equal to the analytic integral of the magnetic energy initially. Finally, the simulation is not performing a single time step, but the conservative time-stepping using RK2-Average scheme is applied with the step $4 \cdot 10^{-4}$, despite the fact that the hydrodynamic motion is still minuscule ($R_m \approx 0.02$).

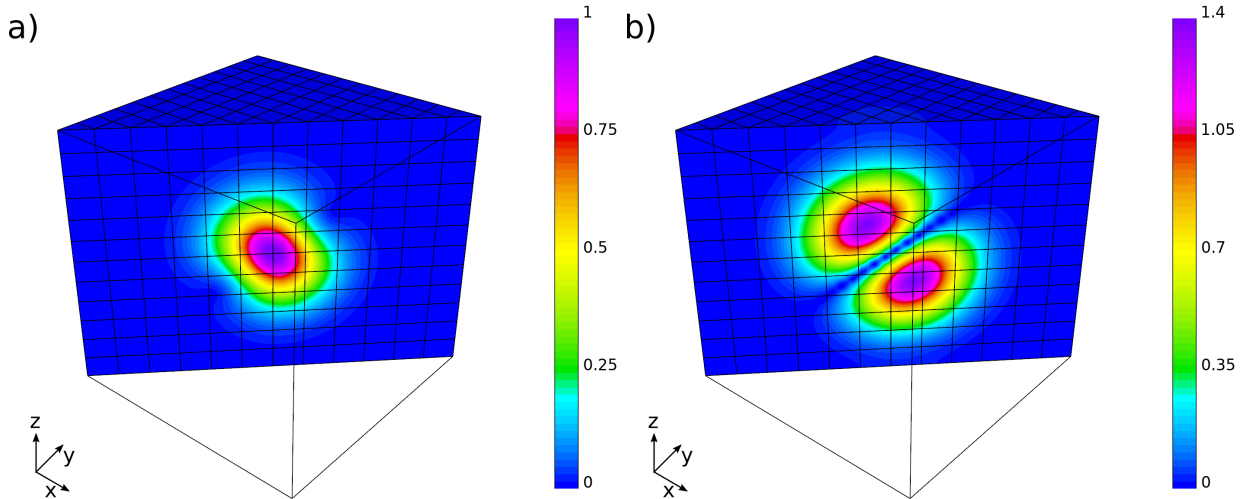


Figure 7: Profiles of electric field (a) and magnetic field (b) in the non-asymptotic magnetic diffusion problem at the final time $t = 0.02$ (in relative units). The computational mesh consists of $12 \times 12 \times 12$ finite elements of the $T3M3$ family.

The given parameters correspond to the dimensionless factor $\eta_m t / \sigma_0^2 \doteq 0.22$, which indicates an advanced state of diffusion. The solution in 3D at the final time is shown in Figure 7. Despite the low number of elements, details of the solution are captured relatively well due to the high order elements used. An asymmetry induced by the divergence term in (37) is apparent too, pointing to the fact that the asymptotic solution (38) is no longer applicable.

Departure from the linear regime is also confirmed by the energy plots in Figure 8. The Joule heating process, converting the magnetic to internal energy, slowly decelerates and ends with the total amount of energy exchanged being about 15 % in 2D and 20 % in 3D. The total energy is conserved throughout the process due to the construction of the scheme (see section 3.2.2). However, this is only true when the Poynting vector term is included in (13e). Although it is neglected in the electrostatic approximation, it arises from the dual formulation of Joule heating in this case. When the term $\mathbb{S}_{ij} \cdot \mathbf{E}_i \mathbf{B}_j$ is omitted, energy conservation is violated, as can be observed on the inset plots of Figure 8. This effect is more pronounced for the higher order elements, which better resolve the gradients. Although the overall effects are quantitatively insignificant (of the order 10^{-4} in 2D and 10^{-3} in 3D), the spatial profiles of specific internal energy differ completely, as can be seen in Figure 9. Essentially, the heating term is then proportional to $\sim \vec{B}^2$ rather than to $\sim \vec{E}^2$ as it is supposed to be. Therefore, the maximum is located at the center of the domain instead of the peripheral area. Moreover, regions of cooling (decreasing energy) can be noticed. This stresses the importance of the Poynting vector term in (13e), which cannot be omitted.

4.4. MHD rotor

The next problem considered is the magneto-hydrodynamic rotor, originating from a simplified model of star formation [37]. A rotating magnetized cylinder emits torsional Alfvénic waves, dissipating its angular momentum through the process. This presents a classical test problem for Eulerian coplanar MHD [38], but rarely for Lagrangian codes, where the computational mesh entangles during the rotation rapidly. However,

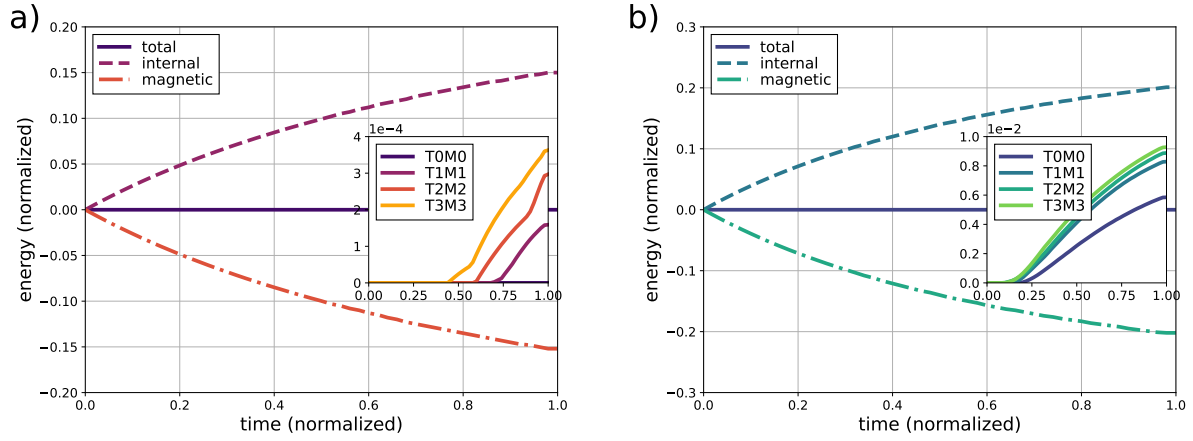


Figure 8: Evolution of total, internal and magnetic energy in the magnetic diffusion problem in 2D (a) and 3D (b). The energies are relative to their initial values and normalized to the value of total energy. Time is normalized to the final time $t = 0.02$. The inset plot shows the total energy deviation for different finite elements for simulations *without* the Poynting vector term. The resolution is 48 $T0M0$, 24 $T1M1$, 16 $T2M2$ and 12 $T3M3$ finite elements in each dimension (the internal and magnetic energy curves are nearly identical and are not distinguished here).

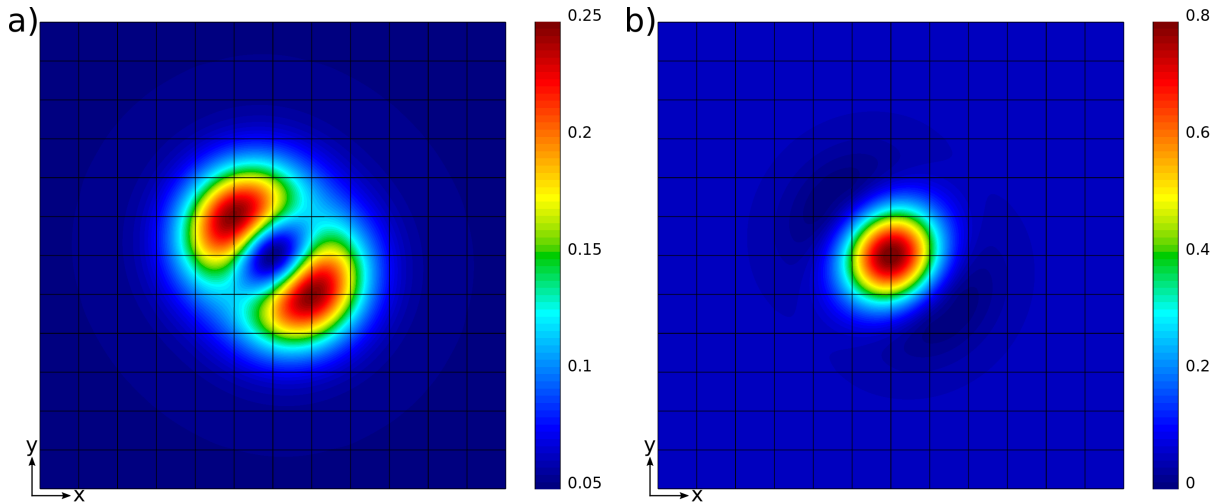


Figure 9: Specific internal energy profiles (in relative units) for the non-asymptotic magnetic diffusion problem in 2D: a) *with* and b) *without* the Poynting vector term. The resolution is 12×12 elements of the $T3M3$ family. The snapshots are taken at the final time $t = 0.02$.

the proposed numerical scheme can benefit from the curvilinear nature of the finite elements avoiding this catastrophic process.

The problem is considered on the 2D computational domain $(-1, 1) \times (-1, 1)$, where the cylinder (with a small slope at the edge) is embedded in an initially static ambient medium. The initial profiles of density and velocity are defined as follows:

$$\rho(x, y) = \begin{cases} 10 & r(x, y) \leq r_0, \\ 1 & r(x, y) \geq r_1, \\ 1 + 9f(r) & r_0 < r(x, y) < r_1, \end{cases} \quad (39a)$$

$$\vec{u}(x, y) = \begin{cases} \vec{0} & r(x, y) \geq r_1, \\ f(r)u_0/\max(r, r_0) \begin{pmatrix} -y \\ x \end{pmatrix} & r(x, y) < r_1, \end{cases} \quad (39b)$$

$$f(r) = (r_1 - r)/(r_1 - r_0), \quad (39c)$$

$$r(x, y) = \sqrt{x^2 + y^2}. \quad (39d)$$

The parameters of the radii and velocity are set to $r_0 = 0.1, r_1 = 0.115, u_0 = 2$. The initial pressure is homogeneous everywhere to start from a static equilibrium with $p \equiv 1$, where the ideal gas equation of state is considered with $\gamma = 1.4$ and $A = 1, Z = 0$. In addition, a homogeneous magnetic field is initially imposed along the horizontal axis with magnitude $B_x = 5/2\sqrt{\mu_0/\pi}$.

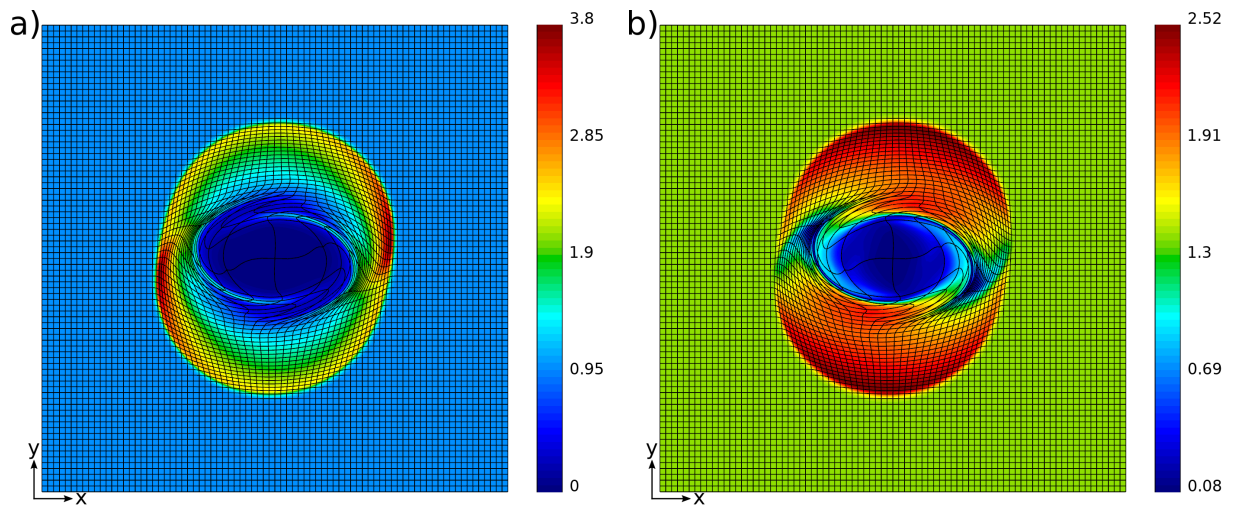


Figure 10: Numerical solution of the MHD rotor problem at the final time $t = 0.15$: a) thermal pressure [relative units] b) magnitude of magnetic field [relative units]. The resolution of the computational mesh is 80×80 finite elements of the $T2M2$ family.

The results for the final time $t = 0.15$ are presented in Figure 10 for a computational mesh composed of 80×80 finite elements from the $T2M2$ family. The time integrating scheme RK3hc(A. α) with CFL equal 0.5 is used (see section 3.3.3). As singularities and strong torsion are present in the solution, the artificial viscosity based on the full eigenvector decomposition is applied [18, 30], where the linear and quadratic coefficients are both equal to 1. The numerical solution shows that even a relatively low number of $T2M2$ finite elements is capable to capture the details without almost any mesh imprint, despite the strong distortion of the mesh, which winds up on the revolving rotor. The tensor artificial viscosity also manifests its strength here, especially in the inner circle around the rotor, where the matter becomes strongly pressed by the magnetic field rather through torsion than normal compression. The shear motion and subsequent

transverse compression is not discriminated in the spectral decomposition and the profiles remain smooth and without any artifacts.

4.5. MHD blast

The final problem presented is the magneto-hydrodynamic blast [39], which was first studied in the astrophysical context as a simplified model of magnetized cosmic jets [40]. Similarly to the classical hydrodynamic problem of Sedov blast [41], a high amount of energy is concentrated in a single point initially, launching a strong blast wave to the ambient medium. The difference is given by the fact that an imposed magnetic field then collimates the blast and competes through the magnetic pressure with the thermal one. The symmetry of the problem around the axis of the magnetic field pre-determines the problem for a study of the geometrical effects in multiple dimensions.

The 3D case is considered, where the simulation box spans over $(-1, 1)^3$ and is filled with an ambient gas of density $\rho \equiv 1$, where the ideal gas EOS is considered with $\gamma = 5/3$ and $A = 1, Z = 0$. The energy equal to the unity is deposited at the center of the domain (as a Dirac function integrally projected onto the mesh), while the background temperature is negligible. As a part of the initial condition, the magnetic field is imposed along the x axis with magnitude $B_x = \sqrt{4/3\mu_0}$.

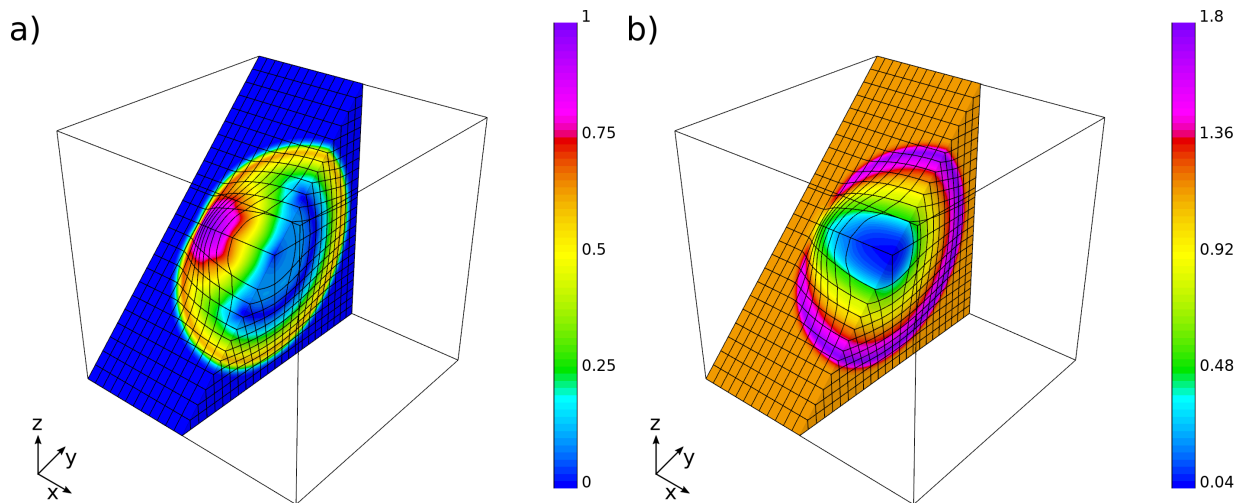


Figure 11: The 3D simulations of MHD blast at the final time $t = 0.25$: a) magnitude of velocity [relative units] b) magnitude of magnetic field [relative units]. The resolution of the computational mesh is $24 \times 24 \times 24$ finite elements of the $T2M2$ family.

The results of the simulations are shown in Figure 11. The computation is performed on a mesh with $24 \times 24 \times 24$ finite elements of the $T2M2$ family. The scheme $RK3hc(A.\alpha)$ is chosen for time integration to match the spatial order according to the findings of section 4.2. The CFL factor is set to 0.5 and the identical model of artificial viscosity as in section 4.4 is applied with the linear coefficient equal to 0.5 and the quadratic to 2. From the numerical profiles, it can be observed that the Lagrangian formulation naturally leads to an increased resolution in the areas of the greatest compression near the fronts of the jets. Therefore, a good level of detail is obtained with a relatively low number of elements and even in 3D the geometric effects on the solution are minimal. The results show the ability of the scheme to treat challenging physical scenarios in multiple dimensions and of relevance to real problems in ICF [1] and astrophysics [5].

5. Discussion

The proposed numerical scheme for conservative Lagrangian magneto-hydrodynamics is presented in section 3, which starts from the general weak formulation (section 3.1) and proceeds towards the fully discrete model (section 3.3). To give a better insight into the construction and outline the future direction

of research, multiple aspects of the scheme are worth of a further discussion, also in the light of the simulation results in section 4.

The weak formulation of section 3.1 established an appealing form of the magneto-hydrodynamic equations (1) for numerical solution. The symmetries between the momentum equation (6a) and the energy equations (6d), (6e) and between the magnetic field equation (6b) and the energy equations already pre-determine the system for a conservative discretization. The specific choices of the functional spaces in section 3.2 and the applied transformation rules guarantee conservation of momentum, magnetic flux and internal energy. In addition, conservation of mass is already given by the geometric conservation law holding for the curvilinear finite elements. The only prize for the total energy conservation is the energy correction term \mathbf{e}_B^c , which accounts for the simultaneous magnetic flux and energy conservation. It also justifies the formulation with the auxiliary equation for magnetic energy (1e). Following the reasoning of section 3.2.1, the definitions of magnetic energy as $\mathbf{1}^T \mathbb{M}_{\mathcal{T}} \mathbf{e}_B$ and $1/(2\mu_0) \mathbf{B}^T \mathbb{M}_{\mathcal{M}} \mathbf{B}$ coincide in absence of motion, but they start to slightly differ for the medium in motion, when the mass matrix $\mathbb{M}_{\mathcal{M}}$ is not constant in contrast to $\mathbb{M}_{\mathcal{T}}$. The correction term \mathbf{e}_B^c defined by (16) is then introduced, which equals to the difference between the increments of the energies given by the two definitions. However, this is not the only possible approach to the problem, as the discrepancy between the energies is tracked due to existence of ε_B and does not need to be explicitly compensated immediately. This idea is elaborated in the symmetrical semi-implicit (SSI) technique suggested in [3], which originates from the context of heat conduction [42]. Since the formulation is already integral within FEM, the advantage of an explicit update is not of an use here (but note the mass matrix $\mathbb{M}_{\mathcal{T}}$ is block-diagonal according to section 3.2.2). Moreover, SSI leads to violation of immediate conservation and energy is conserved only in the limit sense. Therefore, the direct subtraction is preferred.

The time integration procedure described in 3.3.3 employs the second order RK2-Average scheme or the higher order IMEX methods for the ideal magneto-hydrodynamic part of the scheme. All of them are symplectic, conserving kinetic energy and thus the total energy (as internal and magnetic energy are already conserved on the semi-discrete level, see section 3.2). Moreover, the RK2-Average scheme enables to incorporate the magnetodynamic step directly, improving the coupling between the two. Unfortunately, this is not possible for the higher order IMEX methods, which offer symplectic integration without the necessity of implicit solution, but with a drawback of negative time steps appearing in the Butcher tables [27]. This makes the time stepping inapplicable to the diffusion equation of the electric field (25a), since the problem would be ill-posed. For weakly coupled diffusion and convection ($\text{Re}_m \ll 1$ or $\text{Re}_m \gg 1$), the splitting approach, when the magnetodynamic and ideal magneto-hydrodynamic parts are solved separately, is sufficient, but becomes a limiting factor for tightly coupled problems ($\text{Re}_m \sim 1$). Moreover, the magnetodynamic time integration is limited to the second order of convergence. Extension of this part of the scheme to the higher orders is foreseeable by means of singly diagonally implicit Runge-Kutta (SDIRK) methods [43], for example. However, conservation of magnetic energy would be violated this way, as the proof (28) does not hold any longer. Similarly to the ideal MHD part, a symplectic formulation is needed in this case. Thus, conservative high-order methods for the magnetodynamic part and their coupling with the ideal MHD part are topics of the future research.

Despite that the numerical scheme is designed in a rather general and multi-dimensional manner from the beginning, section 3.3.5 narrows the choice of the finite elements to quadrilaterals in 2D and hexahedrals in 3D (note that all elements are curvilinear in general due to the isoparametric mapping). However, this is not required by the construction and is presented only for the sake of brevity and simplicity. An advantage is that the quadrilateral/hexahedral elements are tensorial, where the definitions in the lower and higher dimensions are completely analogous, but simplexes or more complex shapes could be used instead. As far as the conservation properties are considered, the schemes would possess the same features. However, the numerical dispersion relations might differ considerably [44]. On the other hand, simplexes enable conformal h -refinement of the computational mesh, which can increase resolution locally. However, conservation of all thermodynamic and kinematic quantities presents a non-linear problem, which becomes challenging for Lagrangian meshes [45]. Another approach is to perform p -refinement, where the polynomial order of the elements is increased locally [46]. As section 4 shows, the order of convergence is proportional to the order of the elements, indicating that the procedure of p -refinement would bear its fruits. However, the problem of mesh entangling inherent to all Lagrangian models is greatly reduced by the use of the curvilinear finite

elements already. The problem of a MHD rotor in section 4.4 showed that numerical simulations remain feasible even with considerably distorted meshes. For even more dramatic deformations of the mesh, like turbulences or instabilities, the arbitrary Lagrangian–Eulerian (ALE) methods [47] can be employed. Such methods exist for the high-order Lagrangian hydrodynamics [48, 49], but must be non-trivially extended to the proposed MHD model, which presents one of the topics of the future work.

6. Conclusions

Numerical magneto-hydrodynamics is a well-established field of computational physics, but conservative high-order multi-dimensional methods are scarce (with some exceptions for Eulerian methods [14, 15]). The presented Lagrangian numerical scheme based on curvilinear finite elements offers these features. The high-order elements equipped with the isoparametric mapping can track the motion of the simulated magnetized fluid for a long time without getting entangled, as the results of section 4 show. The simulations are also resilient with respect to mesh deformation, exhibiting only minimal mesh imprint. Moreover, the order of spatial convergence is proportional to the polynomial order of the finite elements for smooth problems. Together with the high-order time integration methods of 3.3.3, theoretically an arbitrary order of overall convergence can be attained for ideal MHD. In all cases, exact conservation of mass, momentum, magnetic flux and the total energy is guaranteed by the construction of the elements and scheme according to section 3. Furthermore, the magnetic field remains divergence-free for the whole time span of the simulation.

Altogether, the novel method can push the frontiers of research in ICF [1], astrophysics [5], prepulse effects of ultra-intense lasers [6, 7] or laser ion acceleration beamlines [50, 8, 9, 10] and other areas, where the Lagrangian approach is favored for a strong expansion/compression of the matter and a multi-dimensional treatment is needed. These applications can then benefit from the rapid convergence, flexibility of the mesh design and robustness of the method.

Despite all the attractive features of the scheme, the discussion of section 5 pointed out some limitations of the current design. Among other, it is the fact that the magnetodynamic part of the scheme is not fully coupled with the ideal hydrodynamic part for the higher orders of time integration and remains limited to the second order of convergence. Hence, development of conservative high-order time integration methods for the fully coupled resistive MHD system is a topic of future work. Similarly, advantage of the formulation generality can be taken and methods of *hp*-adaptivity or an ALE model can be proposed. Furthermore, the physical model can be extended by the Nernst effect, thermoelectric effect and others to what is known as the extended MHD model [51], where possible non-locality of the transport should be taken into account [21, 52]. Finally, the topic of self-generated magnetic fields through the process of the Biermann battery can be addressed [53, 54].

Acknowledgments

Portions of this research were carried out at ELI Beamlines, a European user facility operated by the Institute of Physics of the Academy of Sciences of the Czech Republic. Supported by CAAS project CZ.02.1.01/0.0/0.0/16_019/0000778 from European Regional Development Fund; Czech Technical University grant SGS19/191/OHK4/3T/14 and Czech Science Foundation project 19-24619S. The computations were performed using computational resources funded from the CAAS project. This work has received funding from the Eurofusion Enabling Research Project No. CfP-FSD-AWP21-ENR-01-CEA-02.

Stefan Weber was supported by the project Advanced research using high intensity laser produced photons and particles (ADONIS) (CZ.02.1.01/0.0/0.0/16_019/0000789) and by the project High Field Initiative (HiFI) (CZ.02.1.01/0.0/0.0/15_003/0000449), both from European Regional Development Fund.

Appendix A. Equations of magneto-hydrodynamics in 1D and 2D

The differential formulation of the magneto-hydrodynamic equations (5) reduces and splits for the transverse components subscripted by \perp and coplanar/collinear components denoted by the subscript \parallel in 1D

and 2D Cartesian geometry. The equations of mass (5a) and momentum (5b), which do not involve the fields directly, are not affected formally and only the definition of the magnetic stress tensor $\bar{\sigma}_B$ must be modified accordingly.

The 1D formulation requires to define the transverse curl $\nabla_{\perp} \times$ operating on the transverse components of the fields¹. The equations of the magnetic field (5c) and energies (5d), (5e) can then be written as:

$$\frac{d\vec{B}_{\parallel}}{dt} = 0, \quad (\text{A.1a})$$

$$\frac{d\vec{B}_{\perp}}{dt} = -\nabla_{\perp} \times \vec{E}_{\perp} + (\vec{B}_{\parallel} \nabla) \vec{u}_{\perp}, \quad (\text{A.1b})$$

$$\rho \frac{d\varepsilon}{dt} = \bar{\sigma} : \nabla \vec{u} + \vec{j}_{\perp} \cdot \vec{E}_{\perp}, \quad (\text{A.1c})$$

$$\rho \frac{d\varepsilon_B}{dt} = \bar{\sigma}_B : \nabla \vec{u} - \frac{1}{\mu_0} \vec{B}_{\perp} \cdot \nabla_{\perp} \times \vec{E}_{\perp}. \quad (\text{A.1d})$$

In 2D, the curl operators $\nabla_{\parallel} \times$ and $\nabla_{\perp} \times$, crossing between the coplanar and transverse components, are used². The splitted part of the system (5) is then taking the form:

$$\frac{d\vec{B}_{\parallel}}{dt} = -\nabla_{\parallel} \times \vec{E}_{\perp}, \quad (\text{A.2a})$$

$$\frac{d\vec{B}_{\perp}}{dt} = -\nabla_{\perp} \times \vec{E}_{\parallel} + (\vec{B}_{\parallel} \nabla) \vec{u}_{\perp}, \quad (\text{A.2b})$$

$$\rho \frac{d\varepsilon}{dt} = \bar{\sigma} : \nabla \vec{u} + \vec{j}_{\parallel} \cdot \vec{E}_{\parallel} + \vec{j}_{\perp} \cdot \vec{E}_{\perp}, \quad (\text{A.2c})$$

$$\rho \frac{d\varepsilon_B}{dt} = \bar{\sigma}_B : \nabla \vec{u} - \frac{1}{\mu_0} \vec{B}_{\parallel} \cdot \nabla_{\parallel} \times \vec{E}_{\perp} - \frac{1}{\mu_0} \vec{B}_{\perp} \cdot \nabla_{\perp} \times \vec{E}_{\parallel}. \quad (\text{A.2d})$$

Appendix B. Weak formulation in 1D and 2D

The weak formulation following section 3.1 in 1D and 2D requires to define the functional spaces for the transverse and coplanar/collinear components introduced along with the governing equations in Appendix A. The space of scalar thermodynamic potentials $\mathcal{T} \subset L_2(\Omega)$ remains unaffected, while the space of kinematic quantities $\mathcal{K} \subset (H^1(\Omega))^3$ is divided into the coplanar/collinear part $\mathcal{K}_{\parallel} \subset (H^1(\Omega))^d$ and the transverse part $\mathcal{K}_{\perp} \subset (H^1(\Omega))^{3-d}$, where $d \in \{1, 2\}$ is the dimension. The space \mathcal{K}_{\parallel} is used for the coordinates \vec{x} , whereas the velocities \vec{u} are taken from the full space \mathcal{K} in (6a), but only the collinear/coplanar components enter the update of coordinates $d\vec{x}/dt = \vec{u}_{\parallel}$.

Appendix B.1. Weak formulation in 1D

In one dimension, the collinear component of electric field does not exist (with the exception of a non-interacting homogeneous field) and the rest of the spaces is defined as follows:

- collinear magnetic (\mathcal{M}_{\parallel}) – $\mathcal{M}_{\parallel} \subset L_2(\Omega)$,
- transverse magnetic (\mathcal{M}_{\perp}) – $\mathcal{M}_{\perp} \subset (L_2(\Omega))^2$,
- transverse electric (\mathcal{E}_{\perp}) – $\mathcal{E}_{\perp} \subset (H^1(\Omega))^2$.

¹ $\nabla_{\perp} \times = \begin{pmatrix} 0 & -\partial_x \\ \partial_x & 0 \end{pmatrix}$, where x is the 1D coordinate.

² $\nabla_{\parallel} \times = \begin{pmatrix} \partial_y & -\partial_x \end{pmatrix}^T$ and $\nabla_{\perp} \times = \begin{pmatrix} -\partial_y & \partial_x \end{pmatrix}$, where x and y are the 2D coordinates.

The weak formulation of the system (A.1) (without trivial (A.1a)) together with Ohm's law $\vec{E}_\perp = \eta \vec{j}_\perp = \eta/\mu_0 \nabla_\perp \times \vec{B}_\perp$ then takes the form:

$$\int_\Omega \frac{d\vec{B}_\perp}{dt} \cdot \vec{\Xi}_\perp dV = - \int_\Omega \nabla_\perp \times \vec{E}_\perp \cdot \vec{\Xi}_\perp + ((\vec{B}_\parallel \nabla) \vec{u}_\perp) \cdot \vec{\Xi}_\perp dV, \quad \forall \vec{\Xi}_\perp \in \mathcal{M}_\perp, \quad (\text{B.1a})$$

$$\int_\Omega \frac{1}{\eta} \vec{E}_\perp \cdot \vec{\xi}_\perp dV = \int_\Omega \frac{1}{\mu_0} \vec{B}_\perp \cdot \nabla_\perp \times \vec{\xi}_\perp dV - \int_{\Gamma_B} \frac{1}{\mu_0} \vec{B}_\perp^\tau \cdot \vec{\xi}_\perp dS, \quad \forall \vec{\xi}_\perp \in \mathcal{E}_\perp, \quad (\text{B.1b})$$

$$\begin{aligned} \int_\Omega \rho \frac{d\varepsilon}{dt} \varphi dV &= \int_\Omega \bar{\sigma} : \nabla \vec{u} \varphi + \frac{1}{\mu_0} \vec{B}_\perp \cdot \nabla_\perp \times \vec{E}_\perp \varphi + \frac{1}{\mu_0} \vec{E}_\perp \times \vec{B}_\perp \cdot \nabla \varphi dV + \\ &+ \int_{\Gamma_E} \frac{1}{\mu_0} \vec{E}_\perp^\tau \cdot \text{T} \vec{B}_\perp \text{T} \varphi dS - \int_{\Gamma_B} \frac{1}{\mu_0} \vec{E}_\perp \cdot \vec{B}_\perp^\tau \text{T} \varphi dS, \quad \forall \varphi \in \mathcal{T}, \quad (\text{B.1c}) \end{aligned}$$

$$\int_\Omega \rho \frac{d\varepsilon_B}{dt} \varphi dV = \int_\Omega \bar{\sigma}_B : \nabla \vec{u} \varphi - \frac{1}{\mu_0} \vec{B}_\perp \cdot \nabla_\perp \times \vec{E}_\perp \varphi dV, \quad \forall \varphi \in \mathcal{T}. \quad (\text{B.1d})$$

The boundary conditions are analogous to (7), where the conditions for the fields reduce to the transverse components only.

Appendix B.2. Weak formulation in 2D

The two-dimensional formulation involves all components of the fields, which are taken from the following functional spaces:

- coplanar magnetic (\mathcal{M}_\parallel) – $\mathcal{M}_\parallel \subset H_{div}(\Omega)$,
- transverse magnetic (\mathcal{M}_\perp) – $\mathcal{M}_\perp \subset L_2(\Omega)$,
- coplanar electric (\mathcal{E}_\parallel) – $\mathcal{E}_\parallel \subset H_{curl}(\Omega)$,
- transverse electric (\mathcal{E}_\perp) – $\mathcal{E}_\perp \subset H^1(\Omega)$,

The system (A.2) along with Ohm's law $\vec{E}_\parallel = \eta \vec{j}_\parallel = \eta/\mu_0 \nabla_\parallel \times \vec{B}_\perp$ and $\vec{E}_\perp = \eta \vec{j}_\perp = \eta/\mu_0 \nabla_\perp \times \vec{B}_\parallel$ can be formulated in the weak sense as:

$$\int_\Omega \frac{d\vec{B}_\parallel}{dt} \cdot \vec{\Xi}_\parallel dV = - \int_\Omega \nabla_\parallel \times \vec{E}_\perp \cdot \vec{\Xi}_\parallel dV, \quad \forall \vec{\Xi}_\parallel \in \mathcal{M}_\parallel, \quad (\text{B.2a})$$

$$\int_\Omega \frac{d\vec{B}_\perp}{dt} \cdot \vec{\Xi}_\perp dV = - \int_\Omega \nabla_\perp \times \vec{E}_\parallel \cdot \vec{\Xi}_\perp + ((\vec{B}_\parallel \nabla) \vec{u}_\perp) \cdot \vec{\Xi}_\perp dV, \quad \forall \vec{\Xi}_\perp \in \mathcal{M}_\perp, \quad (\text{B.2b})$$

$$\int_\Omega \frac{1}{\eta} \vec{E}_\parallel \cdot \vec{\xi}_\parallel dV = \int_\Omega \frac{1}{\mu_0} \vec{B}_\perp \cdot \nabla_\perp \times \vec{\xi}_\parallel dV - \int_{\Gamma_B} \frac{1}{\mu_0} \vec{B}_\perp^\tau \cdot \vec{\xi}_\parallel dS, \quad \forall \vec{\xi}_\parallel \in \mathcal{E}_\parallel, \quad (\text{B.2c})$$

$$\int_\Omega \frac{1}{\eta} \vec{E}_\perp \cdot \vec{\xi}_\perp dV = \int_\Omega \frac{1}{\mu_0} \vec{B}_\parallel \cdot \nabla_\parallel \times \vec{\xi}_\perp dV - \int_{\Gamma_B} \frac{1}{\mu_0} \vec{B}_\parallel^\tau \cdot \vec{\xi}_\perp dS, \quad \forall \vec{\xi}_\perp \in \mathcal{E}_\perp, \quad (\text{B.2d})$$

$$\begin{aligned} \int_\Omega \rho \frac{d\varepsilon}{dt} \varphi dV &= \int_\Omega \bar{\sigma} : \nabla \vec{u} \varphi + \frac{1}{\mu_0} \vec{B}_\parallel \cdot \nabla_\parallel \times \vec{E}_\perp \varphi dV + \frac{1}{\mu_0} \vec{B}_\perp \cdot \nabla_\perp \times \vec{E}_\parallel \varphi + \\ &+ \frac{1}{\mu_0} \vec{E}_\perp \times \vec{B}_\parallel \cdot \nabla \varphi + \frac{1}{\mu_0} \vec{E}_\parallel \times \vec{B}_\perp \cdot \nabla \varphi dV + \\ &+ \int_{\Gamma_E} \frac{1}{\mu_0} \vec{E}_\perp^\tau \cdot \text{T} \vec{B}_\parallel \text{T} \varphi + \frac{1}{\mu_0} \vec{E}_\parallel^\tau \cdot \text{T} \vec{B}_\perp \text{T} \varphi dS - \\ &- \int_{\Gamma_B} \frac{1}{\mu_0} \vec{E}_\perp \cdot \vec{B}_\parallel^\tau \text{T} \varphi + \frac{1}{\mu_0} \vec{E}_\parallel \cdot \vec{B}_\perp^\tau \text{T} \varphi dS, \quad \forall \varphi \in \mathcal{T}, \quad (\text{B.2e}) \end{aligned}$$

$$\int_\Omega \rho \frac{d\varepsilon_B}{dt} \varphi dV = \int_\Omega \bar{\sigma}_B : \nabla \vec{u} \varphi - \frac{1}{\mu_0} \vec{B}_\parallel \cdot \nabla_\parallel \times \vec{E}_\perp \varphi - \frac{1}{\mu_0} \vec{B}_\perp \cdot \nabla_\perp \times \vec{E}_\parallel \varphi dV, \quad \forall \varphi \in \mathcal{T}. \quad (\text{B.2f})$$

The boundary conditions are analogous to (7), but the components of the fields must be distinguished. The coplanar components of the boundary field values define the transverse boundary data and vice versa, following (7b).

Appendix C. Definitions of the discrete vectors, matrices and tensors

The transition from the weak formulation (6) to the semi-discrete model (13) leads to the definition of the (bi-/tri-)linear forms on the given finite element spaces and their associated vectors/matrices/tensors. In all cases, the integrals are formulated in the real space, i.e., on the moving domain $\Omega(t)$ (and its boundary), and the base functions there are understood as compound functions of the basis function and the reverse map of $\vec{x}(t, \vec{X})$ denoted as $\vec{X}(t, \vec{x})$, i.g. $\varphi(t, \vec{X}) = \varphi(t, \vec{X}(t, \vec{x}))$. However, the integrals are numerically evaluated on Ω_0 for practical purposes, so the inversion of the mapping is not required, but the transformation is obvious and not presented for brevity. The vectors/matrices/tensors are defined as follows:

$$(\mathbb{M}_{\mathcal{T}})_{ij} = \int_{\Omega(t)} \rho \varphi_i \varphi_j \, dV, \quad (\mathbb{M}_{\mathcal{K}})_{ij} = \int_{\Omega(t)} \rho \vec{\psi}_i \cdot \vec{\psi}_j \, dV, \quad (\text{C.1})$$

$$(\mathbb{M}_{\mathcal{M}})_{ij} = \int_{\Omega(t)} \vec{\Xi}_i \cdot \vec{\Xi}_j \, dV, \quad (\mathbb{M}_{\mathcal{E}})_{ij} = \int_{\Omega(t)} \eta^{-1} \vec{\xi}_i \cdot \vec{\xi}_j \, dV, \quad (\text{C.2})$$

$$\mathbb{F}_{ij} = \int_{\Omega(t)} \sigma : \nabla \vec{\psi}_i \varphi_j \, dV, \quad (\mathbb{F}_B)_{ij} = \int_{\Omega(t)} \sigma_B : \nabla \vec{\psi}_i \varphi_j \, dV, \quad (\text{C.3})$$

$$\mathbb{C}_{ijk} = \int_{\Omega(t)} \nabla \times \vec{\xi}_i \cdot \vec{\Xi}_j \varphi_k \, dV, \quad \mathbb{D}_{ij} = \int_{\Omega(t)} \nabla \times \vec{\xi}_i \cdot \nabla \times \vec{\xi}_j \, dV, \quad (\text{C.4})$$

$$(\mathbb{X}_E)_{ij} = \int_{\Gamma_E(t)} \frac{1}{\mu_0} \vec{E}^\tau \cdot \vec{\Xi}_j \varphi_i \, dS, \quad (\mathbb{X}_B)_{ij} = - \int_{\Gamma_B(t)} \frac{1}{\mu_0} \vec{\xi}_j \cdot \vec{B}^\tau \varphi_i \, dS, \quad (\text{C.5})$$

$$(\mathbf{b}_\sigma)_i = \int_{\Gamma_\sigma(t)} \vec{\sigma}_n \cdot \vec{\psi}_i \, dS, \quad (\text{C.6})$$

where the parametric time dependency is omitted for brevity and indexes iterate over all base functions of the given kind. Finally, the tensor of Poynting vector divergence is defined as:

$$\mathbb{S}_{ijk} = \sum_{\Omega_e \in \Sigma_h} \int_{\Omega_e(t)} \frac{1}{\mu_0} \vec{\xi}_i \times \vec{\Xi}_j \cdot \nabla \varphi_k \, dV + \sum_{\Gamma \in \Upsilon_h} \int_{\Gamma(t)} \frac{1}{\mu_0} \vec{\xi}_i \times \{\vec{\Xi}_j\} \cdot \vec{n}[\varphi_k] \, dS. \quad (\text{C.7})$$

The notation utilizes the operators $\{\cdot\}$ for the mean value at the edge and $[\cdot]$ for the normal jump of the quantity across the edge.

Appendix D. Specific spatial discretization in 1D and 2D

Following section 3.3.5, specific choices of the finite element spaces are made in 1D and 2D. In all cases, they are conforming with the corresponding functional spaces used in the weak formulation of Appendix B and an isoparametric mapping is applied on them.

The finite element spaces in 1D are defined as follows:

- thermodynamic – $\mathcal{T}_h = \{\varphi \in \mathcal{T} \mid \varphi|_{\Omega_e} \in P^p(\Omega_e) \quad \forall \Omega_e \in \Sigma_h\}$,
- collinear kinematic – $\mathcal{K}_{\parallel h} = \{\vec{\psi} \in \mathcal{K}_{\parallel} \mid \vec{\psi}|_{\Omega_e} \in P^{p+1}(\Omega_e) \quad \forall \Omega_e \in \Sigma_h\}$,
- transverse kinematic – $\mathcal{K}_{\perp h} = \{\vec{\psi} \in \mathcal{K}_{\perp} \mid \vec{\psi}|_{\Omega_e} \in (P^{p+1}(\Omega_e))^2 \quad \forall \Omega_e \in \Sigma_h\}$,
- collinear magnetic – $\mathcal{M}_{\parallel h} = \{\vec{\Xi} \in \mathcal{M}_{\parallel} \mid \vec{\Xi}|_{\Omega_e} \in P^q(\Omega_e) \quad \forall \Omega_e \in \Sigma_h\}$,

- transverse magnetic – $\mathcal{M}_{\perp h} = \{\vec{\Xi} \in \mathcal{M}_{\perp} \mid \vec{\Xi}|_{\Omega_e} \in (P^q(\Omega_e))^2 \quad \forall \Omega_e \in \Sigma_h\}$,
- transverse electric – $\mathcal{E}_{\perp h} = \{\vec{\xi} \in \mathcal{E}_{\perp} \mid \vec{\xi}|_{\Omega_e} \in (P^{q+1}(\Omega_e))^2 \quad \forall \Omega_e \in \Sigma_h\}$.

In two dimensions, the definitions are following:

- thermodynamic – $\mathcal{T}_h = \{\varphi \in \mathcal{T} \mid \varphi|_{\Omega_e} \in Q^p(\Omega_e) \quad \forall \Omega_e \in \Sigma_h\}$,
- coplanar kinematic – $\mathcal{K}_{\parallel h} = \{\vec{\psi} \in \mathcal{K}_{\parallel} \mid \vec{\psi}|_{\Omega_e} \in (Q^{p+1}(\Omega_e))^2, \vec{\psi}|_{\Gamma_e} \in (P^{p+1}(\Omega_e))^2 \quad \forall \Omega_e \in \Sigma_h, \Gamma_e \subset \partial\Omega_e\}$,
- transverse kinematic – $\mathcal{K}_{\perp h} = \{\vec{\psi} \in \mathcal{K}_{\perp} \mid \vec{\psi}|_{\Omega_e} \in Q^{p+1}(\Omega_e), \vec{\psi}|_{\Gamma_e} \in P^{p+1}(\Omega_e) \quad \forall \Omega_e \in \Sigma_h, \Gamma_e \subset \partial\Omega_e\}$,
- coplanar magnetic – $\mathcal{M}_{\parallel h} = \{\vec{\Xi} \in \mathcal{M}_{\parallel} \mid \vec{\Xi}|_{\Omega_e} \in RT_{2D}^{q+1}(\Omega_e) \quad \forall \Omega_e \in \Sigma_h\}$,
- transverse magnetic – $\mathcal{M}_{\perp h} = \{\vec{\Xi} \in \mathcal{M}_{\perp} \mid \vec{\Xi}|_{\Omega_e} \in Q^q(\Omega_e) \quad \forall \Omega_e \in \Sigma_h\}$,
- coplanar electric – $\mathcal{E}_{\parallel h} = \{\vec{\xi} \in \mathcal{E}_{\parallel} \mid \vec{\xi}|_{\Omega_e} \in ND_{2D}^{q+1}(\Omega_e) \quad \forall \Omega_e \in \Sigma_h\}$,
- transverse electric – $\mathcal{E}_{\perp h} = \{\vec{\xi} \in \mathcal{E}_{\perp} \mid \vec{\xi}|_{\Omega_e} \in Q^{q+1}(\Omega_e), \vec{\xi}|_{\Gamma_e} \in P^{q+1}(\Omega_e) \quad \forall \Omega_e \in \Sigma_h, \Gamma_e \subset \partial\Omega_e\}$,

where P^p are polynomials up to the order p . The polynomials RT_{2D}^{p+1} and ND_{2D}^{p+1} are Raviart–Thomas H_{div} conforming and Nédélec H_{curl} conforming finite elements in 2D [55, 31]. The sets Γ_e represent the edges of the element Ω_e in this context.

References

- [1] L. J. Perkins, D. D. Ho, B. G. Logan, G. B. Zimmerman, M. A. Rhodes, D. J. Strozzi, D. T. Blackfield, S. A. Hawkins, The potential of imposed magnetic fields for enhancing ignition probability and fusion energy yield in indirect-drive inertial confinement fusion, *Physics of Plasmas* 24 (6) (2017) 062708. doi:10.1063/1.4985150.
- [2] D. S. Clark, M. M. Marinak, C. R. Weber, D. C. Eder, S. W. Haan, B. A. Hammel, D. E. Hinkel, O. S. Jones, J. L. Milovich, P. K. Patel, H. F. Robey, J. D. Salmonson, S. M. Sepke, C. A. Thomas, Radiation hydrodynamics modeling of the highest compression inertial confinement fusion ignition experiment from the National Ignition Campaign, *Physics of Plasmas* 22 (2) (2015) 1–19. doi:10.1063/1.4906897.
- [3] F. Wu, R. Ramis, Z. Li, A conservative MHD scheme on unstructured Lagrangian grids for Z-pinch hydrodynamic simulations, *Journal of Computational Physics* 357 (2018) 206–229. doi:10.1016/j.jcp.2017.12.014.
- [4] E. Livne, A. Burrows, R. Walder, I. Lichtenstadt, T. A. Thompson, Two-dimensional, time-dependent, multigroup, multiangle radiation hydrodynamics test simulation in the core-collapse supernova context, *The Astrophysical Journal* 609 (1) (2004) 277–287. doi:10.1086/421012.
- [5] R. E. Pudritz, M. J. Hardcastle, D. C. Gabuzda, Magnetic fields in astrophysical jets: From launch to termination, *Space Science Reviews* 169 (1-4) (2012) 27–72. doi:10.1007/s11214-012-9895-z.
- [6] J. Nikl, M. Jirka, M. Kucharík, M. Holec, M. Vranic, S. Weber, The effect of pre-plasma formed under the non-local transport conditions on the interaction of the ultra-high intensity laser with a solid target, in: *Research using Extreme Light: Entering New Frontiers with Petawatt-Class Lasers IV*, Vol. 11039 of *Proceedings of SPIE*, 2019, p. 110391E. doi:10.1117/12.2522450.
- [7] M. Holec, J. Nikl, M. Vranic, S. Weber, The effect of pre-plasma formation under nonlocal transport conditions for ultra-relativistic laser-plasma interaction, *Plasma Physics and Controlled Fusion* 60 (4) (2018) 044019. doi:10.1088/1361-6587/aab05a.
- [8] J. Psikal, Laser-driven ion acceleration from near-critical Gaussian plasma density profile, *Plasma Physics and Controlled Fusion* 63 (6) (2021) 064002. doi:10.1088/1361-6587/abf448.
- [9] J. Psikal, V. Horny, M. Zakova, M. Matys, Comparison of ion acceleration from nonexpanded and expanded thin foils irradiated by ultrashort petawatt laser pulse, in: E. Esarey, C. B. Schroeder, J. Schreiber (Eds.), *Laser Acceleration of Electrons, Protons, and Ions V*, Vol. 11037 of *Proceedings of SPIE*, 2019, pp. 7 – 13. doi:10.1117/12.2520278.
- [10] D. Batani, R. Jafer, M. Veltcheva, R. Dezulian, O. Lundh, F. Lindau, A. Persson, K. Osvay, C. G. Wahlström, D. C. Carroll, P. McKenna, A. Flacco, V. Malka, Effects of laser prepulses on laser-induced proton generation, *New Journal of Physics* 12. doi:10.1088/1367-2630/12/4/045018.
- [11] S. Weber, S. Bechet, S. Borneis, L. Brabec, M. Bučka, E. Chacon-Golcher, M. Ciappina, M. DeMarco, A. Fajstavr, K. Falk, E.-R. Garcia, J. Grosz, Y.-J. Gu, J.-C. Hernandez, M. Holec, P. Janečka, M. Jantač, M. Jirka, H. Kadlecova, D. Khikhlikha, O. Klimo, G. Korn, D. Kramer, D. Kumar, T. Lastovička, P. Lutoslawski, L. Morejon, V. Olšovcová, M. Rajdl, O. Renner, B. Rus, S. Singh, M. Šmid, M. Sokol, R. Versaci, R. Vrána, M. Vranic, J. Vyskočil, A. Wolf, Q. Yu, P3: an installation for high-energy density plasma physics and ultra-high intensity laser-matter interaction at ELI-Beamlines, *Matter and Radiation at Extremes* 2 (2017) 149.

- [12] The Extreme Light Infrastructure project: ELI Beamlines, <http://www.eli-beams.eu>.
- [13] C. N. Danson, C. Haefner, J. Bromage, T. Butcher, J.-C. F. Chanteloup, E. A. Chowdhury, A. Galvanauskas, L. A. Gizzi, J. Hein, D. I. Hillier, N. W. Hopps, Y. Kato, E. A. Khazanov, R. Kodama, G. Korn, R. Li, Y. Li, J. Limpert, J. Ma, C. H. Nam, D. Neely, D. Papadopoulos, R. R. Penman, L. Qian, J. J. Rocca, A. A. Shaykin, C. W. Siders, C. Spindloe, S. Szatmári, R. M. G. M. Trines, J. Zhu, P. Zhu, J. D. Zuegel, Petawatt and exawatt class lasers worldwide, *High Power Laser Science and Engineering* 7 (2019) e54. doi:10.1017/hpl.2019.36.
- [14] D. S. Balsara, M. Dumbser, Divergence-free MHD on unstructured meshes using high order finite volume schemes based on multidimensional Riemann solvers, *Journal of Computational Physics* 299 (2015) 687–715. doi:10.1016/j.jcp.2015.07.012.
- [15] A. Susanto, L. Ivan, H. De Sterck, C. Groth, High-order central ENO finite-volume scheme for ideal MHD, *Journal of Computational Physics* 250 (2013) 141–164. doi:10.1016/j.jcp.2013.04.040.
- [16] R. N. Rieben, D. A. White, B. K. Wallin, J. M. Solberg, An arbitrary Lagrangian–Eulerian discretization of MHD on 3D unstructured grids, *Journal of Computational Physics* 226 (1) (2007) 534–570. doi:10.1016/j.jcp.2007.04.031.
- [17] G. Tóth, The $\nabla \cdot \mathbf{B} = 0$ constraint in shock-capturing magnetohydrodynamics codes, *Journal of Computational Physics* 161 (2) (2000) 605–652. doi:10.1006/jcph.2000.6519.
- [18] V. A. Dobrev, T. V. Kolev, R. N. Rieben, High-order curvilinear finite element methods for Lagrangian hydrodynamics, *SIAM Journal on Scientific Computing* 34 (5) (2012) B606–B641. doi:10.1137/120864672.
- [19] J. Nikl, M. Kuchařík, M. Holec, S. Weber, Curvilinear high-order Lagrangian hydrodynamic code for the laser-target interaction, in: S. Coda, J. Berndt, G. Lapenta, M. Mantsinen, C. Michaut, S. Weber (Eds.), *Europhysics Conference Abstracts – 45th EPS Conference on Plasma Physics*, Vol. 42A, European Physical Society, 2018, p. P1.2019.
- [20] J. Nikl, M. Holec, M. Zeman, M. Kuchařík, J. Limpouch, S. Weber, Macroscopic laser-plasma interaction under strong non-local transport conditions for coupled matter and radiation, *Matter and Radiation at Extremes* 3 (2018) 110–126. doi:10.1016/j.mre.2018.03.001.
- [21] M. Holec, J. Nikl, S. Weber, Nonlocal transport hydrodynamic model for laser heated plasmas, *Physics of Plasmas* 25 (3) (2018) 032704. doi:10.1063/1.5011818.
- [22] M. Lax, D. F. Nelson, Maxwell equations in material form, *Physical Review B* 13 (1976) 1777–1784. doi:10.1103/PhysRevB.13.1777.
- [23] D. N. Arnold, R. S. Falk, R. Winther, Differential complexes and stability of finite element methods I. The de Rham complex, in: D. N. Arnold, P. B. Bochev, R. B. Lehoucq, R. A. Nicolaides, S. M. (Eds.), *Compatible Spatial Discretizations*, Springer New York, New York, NY, 2006, pp. 23–46. doi:10.1007/0-387-38034-5_2.
- [24] R. N. Rieben, D. A. White, Verification of high-order mixed finite-element solution of transient magnetic diffusion problems, *IEEE Transactions on Magnetics* 42 (1) (2006) 25–39. doi:10.1109/TMAG.2005.860127.
- [25] D. Boffi, F. Brezzi, M. Fortin, *Mixed finite element methods and applications*, Vol. 44, Springer, 2013.
- [26] P. D. Thomas, C. K. Lombard, Geometric conservation law and its application to flow computations on moving grids, *AIAA Journal* 17 (10) (1979) 1030–1037. doi:10.2514/3.61273.
- [27] A. Sandu, V. Tomov, L. Cervena, T. Kolev, Conservative high-order time integration for lagrangian hydrodynamics, *SIAM Journal on Scientific Computing* 43 (1) (2021) A221–A241. doi:10.1137/20M1314495.
- [28] M. Torrilhon, Uniqueness conditions for Riemann problems of ideal magnetohydrodynamics, *Journal of Plasma Physics* 69 (3) (2003) 253–276. doi:10.1017/S0022377803002186.
- [29] E. J. Caramana, M. J. Shashkov, P. P. Whalen, Formulations of artificial viscosity for multi-dimensional shock wave computations, *Journal of Computational Physics* 144 (1) (1998) 70–97. doi:10.1006/jcph.1998.5989.
- [30] T. V. Kolev, R. N. Rieben, A tensor artificial viscosity using a finite element approach, *Journal of Computational Physics* 228 (22) (2009) 8336 – 8366. doi:https://doi.org/10.1016/j.jcp.2009.08.010.
- [31] J. C. Nedelec, Mixed finite elements in R3, *Numerische Mathematik* 35 (3) (1980) 315–341. doi:10.1007/BF01396415.
- [32] J. Glaubitz, Shock capturing by Bernstein polynomials for scalar conservation laws, *Applied Mathematics and Computation* 363 (2019) 124593. doi:https://doi.org/10.1016/j.amc.2019.124593.
- [33] MFEM: Modular finite element methods library, <https://mfem.org>. doi:10.11578/dc.20171025.1248.
- [34] R. Anderson, J. Andrej, A. Barker, J. Bramwell, J.-S. Camier, J. Cervený, V. Dobrev, Y. Dudouit, A. Fisher, T. Kolev, W. Pazner, M. Stowell, V. Tomov, I. Akkerman, J. Dahm, D. Medina, S. Zampini, MFEM: A modular finite element methods library, *Computers & Mathematics with Applications* doi:10.1016/j.camwa.2020.06.009.
- [35] GLVis: OpenGL finite element visualization tool, <https://glvis.org>. doi:10.11578/dc.20171025.1249.
- [36] M. Torrilhon, Exact solver and uniqueness conditions for riemann problems of ideal magnetohydrodynamics, *Research report 2002-06*, ETH Zurich (2002). doi:10.3929/ETHZ-A-004339390.
- [37] T. C. Mouschovias, E. V. Paleologou, Magnetic braking of an aligned rotator during star formation: An exact, time-dependent solution, *The Astrophysical Journal* 237 (1980) 877–899.
- [38] D. S. Balsara, D. S. Spicer, A staggered mesh algorithm using high order Godunov fluxes to ensure solenoidal magnetic fields in magnetohydrodynamic simulations, *Journal of Computational Physics* 149 (2) (1999) 270–292. doi:10.1006/jcph.1998.6153.
- [39] A. L. Zachary, A. Malagoli, P. Colella, A higher-order Godunov method for multidimensional ideal magnetohydrodynamics, *SIAM Journal on Scientific Computing* 15 (2) (1994) 263–284. doi:10.1137/0915019.
- [40] D. Kössl, E. Müller, W. Hillebrandt, Numerical simulations of axially symmetric magnetized jets. I : The influence of equipartition magnetic fields, *Astronomy and astrophysics* 229 (2) (1990) 378–396.
- [41] L. I. Sedov, *Similarity and dimensional methods in mechanics*, CRC press, 1993.
- [42] E. Livne, A. Glasner, A finite difference scheme for the heat conduction equation, *Journal of Computational Physics* 58 (1) (1985) 59–66. doi:10.1016/0021-9991(85)90156-1.

- [43] L. Ferracina, M. N. Spijker, Strong stability of singly-diagonally-implicit Runge–Kutta methods, *Applied Numerical Mathematics* 58 (11) (2008) 1675–1686. doi:10.1016/j.apnum.2007.10.004.
- [44] G. S. Warren, W. R. Scott, Numerical dispersion of higher order nodal elements in the finite-element method, *IEEE Transactions on Antennas and Propagation* 44 (3) (1996) 317–320. doi:10.1109/8.486299.
- [45] R. W. Anderson, N. S. Elliott, R. B. Pember, An arbitrary Lagrangian–Eulerian method with adaptive mesh refinement for the solution of the Euler equations, *Journal of Computational Physics* 199 (2) (2004) 598–617. doi:10.1016/j.jcp.2004.02.021.
- [46] A. K. Karanam, A p-adaptive stabilized finite element method for fluid dynamics, Ph.D. thesis, Rensselaer Polytechnic Institute (2008).
- [47] A. J. Barlow, P.-H. Maire, W. J. Rider, R. N. Rieben, M. J. Shashkov, Arbitrary Lagrangian–Eulerian methods for modeling high-speed compressible multimaterial flows, *Journal of Computational Physics* 322 (2016) 603–665. doi:10.1016/j.jcp.2016.07.001.
- [48] H. Hajduk, D. Kuzmin, T. Kolev, V. Tomov, I. Tomas, J. N. Shadid, Matrix-free subcell residual distribution for Bernstein finite elements: Monolithic limiting, *Computers & Fluids* 200 (2020) 104451. doi:10.1016/j.compfluid.2020.104451.
- [49] R. W. Anderson, V. A. Dobrev, T. V. Kolev, R. N. Rieben, V. Z. Tomov, High-order multi-material ALE hydrodynamics, *SIAM Journal on Scientific Computing* 40 (1) (2018) B32–B58. doi:10.1137/17M1116453.
- [50] A. Arefiev, T. Toncian, G. Fiksel, Enhanced proton acceleration in an applied longitudinal magnetic field, *New Journal of Physics* 18 (10) (2016) 105011. doi:10.1088/1367-2630/18/10/105011.
- [51] C. A. Walsh, J. P. Chittenden, D. W. Hill, C. Ridgers, Extended-magnetohydrodynamics in under-dense plasmas, *Physics of Plasmas* 27 (2) (2020) 022103. doi:10.1063/1.5124144.
- [52] C. P. Ridgers, R. J. Kingham, A. G. R. Thomas, Magnetic cavitation and the reemergence of nonlocal transport in laser plasmas, *Physical Review Letters* 100 (7) (2008) 075003. doi:10.1103/PhysRevLett.100.075003.
- [53] J. Nikl, M. Kuchařík, S. Weber, Self-generated magnetic fields modelling within high-order Lagrangian magneto-hydrodynamics, in: *Europhysics Conference Abstracts – 47th EPS Conference on Plasma Physics*, European Physical Society, 2021, p. P1.2022.
- [54] P. Tzeferacos, M. Fatenejad, N. Flocke, C. Graziani, G. Gregori, D. Q. Lamb, D. Lee, J. Meinecke, A. Scopatz, K. Weide, FLASH MHD simulations of experiments that study shock-generated magnetic fields, *High Energy Density Physics* 17 (2015) 24–31. doi:10.1016/j.hedp.2014.11.003.
- [55] P. Lasaint, P. A. Raviart, On a finite element method for solving the neutron transport equation, in: *Mathematical Aspects of Finite Elements in Partial Differential Equations*, Vol. 33, Elsevier, 1974, pp. 89–123. doi:10.1016/B978-0-12-208350-1.50008-X.